Moored Observations of the Surface Meteorology and Air–Sea Fluxes in the Northern Bay of Bengal in 2015

R. A. WELLER, J. T. FARRAR, AND HYODAE SEO

Woods Hole Oceanographic Institution, Woods Hole, Massachusetts

CHANNING PREND

Scripps Institution of Oceanography, La Jolla, California

DEBASIS SENGUPTA AND J. SREE LEKHA

Center for Atmospheric and Oceanic Sciences, Indian Institute of Science, Bangalore, India

M. RAVICHANDRAN

National Centre for Polar and Ocean Research, Goa, India

R. VENKATESEN

National Institute of Ocean Technology, Chennai, India

ABSTRACT

Time series of surface meteorology and air–sea fluxes from the northern Bay of Bengal are analyzed, quantifying annual and seasonal means, variability, and the potential for surface fluxes to contribute significantly to variability in surface temperature and salinity. Strong signals were associated with solar insolation and its modulation by cloud cover, and, in the 5- to 50-day range, with intraseasonal oscillations (ISOs). The northeast (NE) monsoon (DJF) was typically cloud free, with strong latent heat loss and several moderate wind events, and had the only seasonal mean ocean heat loss. The spring intermonsoon (MAM) was cloud free and had light winds and the strongest ocean heating. Strong ISOs and Tropical Cyclone Komen were seen in the southwest (SW) monsoon (JJA), when 65% of the 2.2-m total rain fell, and oceanic mean heating was small. The fall intermonsoon (SON) initially had moderate convective systems and mean ocean heating, with a transition to drier winds and mean ocean heat loss in the last month. Observed surface freshwater flux applied to a layer of the observed thickness produced drops in salinity with timing and magnitude similar to the initial drops in salinity in the summer monsoon, but did not reproduce the salinity variability of the fall intermonsoon. Observed surface heat flux has the potential to cause the temperature trends of the different seasons, but uncertainty in how shortwave radiation is absorbed in the upper ocean limits quantifying the role of surface forcing in the evolution of mixed layer temperature.

1. Introduction

The Bay of Bengal is an extremely challenging region from the perspectives of understanding coupled ocean–atmosphere dynamics, building improved capabilities to predict surface and upper ocean conditions, and including

ⓐ Denotes content that is immediately available upon publication as open access.

Corresponding author: Dr. Robert A. Weller, rweller@whoi.edu

realistic atmosphere–ocean interactions in monsoon prediction models. Much remains to be learned about the surface meteorology and the exchanges of heat, freshwater, and momentum between the ocean and atmosphere. One illustration of that comes from the finding that surface fluxes from existing numerical weather prediction (NWP) and climate models differ greatly in the Bay of Bengal, even to the extent of that some have the opposite sign in the annual mean net heat flux (Yu et al. 2007). Biases in net heat flux in some products are as high as $100\,\mathrm{W\,m}^{-2}$. As a result of the uncertainty, further progress on understanding the coupled

ocean–atmosphere interaction in the Bay of Bengal requires improved quantification of the surface meteorology and the air–sea fluxes of heat, freshwater, and momentum.

Recently, in recognition of the need for observations, there has been work on an Indian Ocean observing system. International collaboration developed the plan for the Research Moored Array for African–Asian–Australian Monsoon Analysis and Prediction (RAMA) and implementation of that array (McPhaden et al. 2009). The Indian National Institute of Ocean Technology (NIOT) is developing and maintaining the Ocean Moored Buoy Network for the Northern Indian Ocean (OMNI), with surface moorings in the Arabian Sea and the Bay of Bengal (Venkatesan et al. 2013). In addition, the desire to improve understanding of air–sea interactions, the variability of the upper ocean, and the role of atmosphere–ocean coupling in monsoons has led to field campaigns to collect more detailed observations and conduct process studies. Recent efforts build upon earlier field programs, including MONEX (the Monsoon Experiment, conducted in 1977; Murakami 1979), BOBMEX (the Bay of Bengal Monsoon Experiment, in 1999; Bhat et al. 2001), and JASMINE (the Joint Air–Sea Interaction Monsoon Experiment, in the eastern Indian Ocean and Southern Bay of Bengal in summer 1999; Webster et al. 2002). Mahadevan et al. (2016) introduce two recent programs, including the Air–Sea Interactions Regional Initiative (ASIRI), supported by the U.S. Office of Naval Research and the Ocean Mixing and Monsoon (OMM) project, part of the Indian Monsoon Mission supported by the Indian Ministry of Earth Science. The ASIRI and OMM programs were carried out in close coordination.

In late 2014, as part of the ASIRI–OMM partnership, a surface mooring was deployed at 18°N, 89.5°E, north of the RAMA array and near OMNI array sites BD08 and BD09. The deployment was done from the Indian Research Vessel (RV) *Sagar Nidhi*; the recovery was done from the Indian RV *Sagar Kanya*. The buoy carried meteorological instrumentation that allowed estimation of the air–sea fluxes of heat, freshwater, and momentum. Data were recorded every minute to capture high-frequency variability, and the deployment extended over 14 months to observe seasonal variability and to examine annual means. In this paper the data are used to describe the surface meteorology and air–sea fluxes of heat, freshwater, and momentum. The observed variability in the surface meteorology and air–sea fluxes are described through a full annual cycle, with attention to the different summer and winter monsoon seasons as well as to the intermonsoon periods. Seasonal mean values are presented to contrast the different seasons. Attention is also paid to variability at diurnal and subseasonal time scales.

Many discussions of the surface meteorology and air–sea fluxes (e.g., Yu et al. 2007) and ocean model studies (e.g., Dey et al. 2017) in the Bay of Bengal have focused on seasonal and longer time scales or have relied on monthly fluxes as forcing. Others (e.g., Narvekar and Kumar 2006) have used monthly means in discussing forcing and ocean response. This paper seeks to complement that work by focusing on the new time series of surface meteorology and air–sea fluxes and including discussion of the higher-frequency variability and its contribution to the air–sea fluxes. At the same time seasons were chosen as four 3-month periods, so that seasonal means presented here could be contrasted to seasonal means computed from previously presented monthly climatologies and data. The winter or northeast (NE) monsoon season was taken as December–February (DJF); the spring intermonsoon came during March–May (MAM); the summer or SW monsoon occurred during June–August (JJA); and the fall intermonsoon season was during September–November (SON).

This work builds on previous efforts to explore the ocean dynamics and to collect time series from moorings in the Bay of Bengal, as, for example, in mooring deployments begun in the late 1990s (e.g., Bhat et al. 2001). This paper follows up the recent work of Sengupta et al. (2016), who described data from a mooring deployed at close to the same location from November 2009 to November 2010. The surface forcing from the mooring discussed here was briefly summarized in Weller et al. (2016); here we discuss it in detail, highlight higher-frequency variability, and investigate the differences between the seasons. This is done to fully characterize the surface meteorology and air–sea fluxes at the site and also to provide documentation to facilitate their use in other studies. To set the stage for assessing the importance of the surface forcing to the temporal evolution of the upper ocean in the northern Bay of Bengal over the year, the annual accumulation of freshwater based on observed precipitation and evaporation, the annual accumulation of heat, and the annual accumulation of wind stress are examined. Then, the observed surface forcing is applied to different models of the surface mixed layer to contrast the resulting mixed layer temperatures and salinity with the corresponding observations from the buoy. These results illustrate the potential for the surface fluxes to contribute significantly to the annual cycle of surface temperature and salinity in the northern Bay of Bengal.

2. The WHOI surface mooring in the northern Bay of Bengal

The site of the surface mooring, 18°N, 89.5°E, was chosen to be in the northern end of the region of international
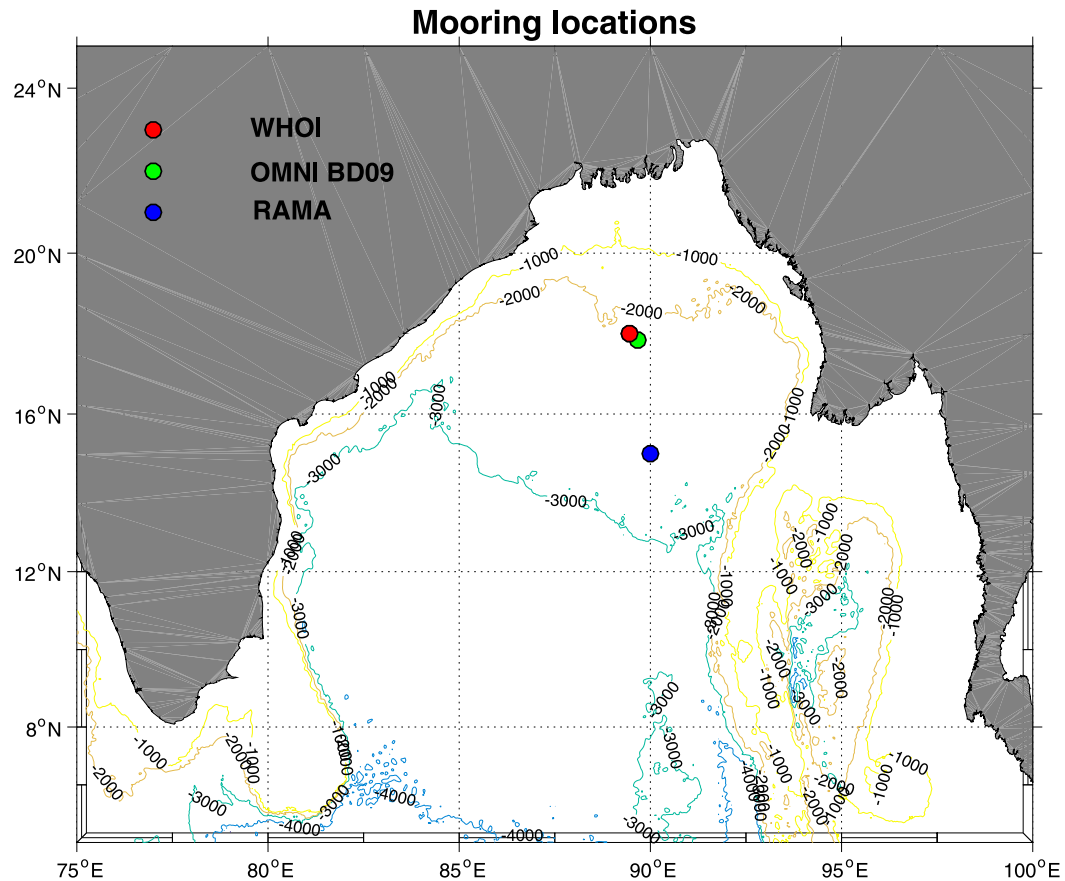
Mooring locations

FIG. 1. Map of the northern Bay of Bengal showing the location of the Woods Hole Oceanographic Institution (WHOI) surface mooring (red) and of the nearby OMNI mooring (BD09) (green) and the northernmost RAMA mooring along 90°E (blue). Bathymetry is in meters.

waters along the center of the Bay of Bengal, in the vicinity of an OMNI mooring (Venkatesan et al. 2013), and to the north of one of the RAMA moorings (McPhaden et al. 2009) (Fig. 1). The mooring was deployed on 8 December 2014 and recovered on 29 January 2016. The surveyed anchor position was 18°00.60′N, 89°27.29′E, and the surface buoy typically stayed within 2 km of the anchor location.

A photograph (Fig. 2) shows the surface buoy just after its deployment. The surface buoy carried two redundant ASIMET (Air–Sea Interaction Meteorological) instruments (Hosom et al. 1995), which each sampled a suite of meteorological and sea surface sensors and recorded averages of those samples once per minute. The sensors were mounted about 3 m above the sea surface and measured wind speed and direction, air temperature and humidity, incoming shortwave radiation, incoming longwave radiation, barometric pressure, and rain rate. Each ASIMET instrument also had a Sea-Bird SBE 37 temperature and conductivity

recorder under the buoy hull at about 1-m depth to provide near-surface temperature and salinity. To supplement the two ASIMET instruments, a Vaisala WXT 520 was mounted on the buoy tower; this sampled wind speed and direction, barometric pressure, precipitation, air temperature, and air humidity. All ASIMET sensors as well as the WXT 520 were calibrated prior to deployment, and the assembled buoy was run on shore prior to shipping and checked for accuracy and any indication of problems such as radio frequency interference. After recovery, the raw 1-min data were downloaded from the ASIMET dataloggers as well as the data from the WXT-520, additional temperature recorders, and Sea-Bird SBE 37s. These data were used to develop a single 1-min time series of surface meteorology as the starting point for this analysis. The mooring line below the buoy carried oceanographic instruments measuring temperature, salinity, and currents. This paper uses density computed from these instruments to obtain a time series of the depth of the ocean surface mixed layer; further

FIG. 2. The surface buoy just after deployment in December 2014, with RV *Sagar Nidhi* in the background. (Photo by Sean Whelan, WHOI)

analyses of the oceanic data are beyond the scope of this paper.

3. Overview of the surface meteorological data and the air–sea fluxes of heat, freshwater, and momentum

During the preparation of the complete, 1-min surface meteorological dataset, no gaps or unresolved sensor drift or bias issues arose. More detail about the sensors and their uncertainties is given in Colbo and Weller (2009), Bigorre et al. (2013), and Weller (2015). In this paper, unless noted, surface meteorological variables are presented as observed at the height of the sensors on the buoy. Following practices developed in the Coupled Ocean–Atmosphere Response Experiment (COARE), when methods for computing air–sea fluxes were intercompared and refined (Weller and Anderson 1996), net shortwave radiation was computed using an albedo of 0.055 and net longwave radiation was computed as $\varepsilon \sigma T_s^4$ minus ε times the observed incoming longwave, where ε is the emissivity at 0.97, σ is the Boltzmann constant at $5.67 \times 10^{-8}\,\mathrm{W\,m^{-2}\,K^{-4}}$, and T_s is the sea surface temperature [including the cool skin and warm-layer corrections of Fairall et al. (1996) to account for the measurement depth

of the sensor, which was about 1 m deep]. Sensible and latent heat flux and wind stress were computed using the COARE bulk formulas that account for atmospheric stability as described by Fairall et al. (2003). During the computation of the fluxes, values of air temperature and humidity extrapolated to 2-m height and wind velocity to 10-m height were saved, and, are provided in summary tables later in the paper for comparison to model-based values. Positive heat flux values indicate heat is going into the ocean. The heat flux associated with rain falling on the ocean is computed in the bulk formula code based on the assumption that rain when it hits the sea surface is at the wet bulb temperature (Gosnell et al. 1995). One-hour, 1-day, and 1-month averaged flux files were made from the 1-min file. Figure 3 provides an overview of the surface meteorology at the mooring. Figure 4 provides an overview of the air–sea fluxes observed at the mooring. Both Fig. 3 and Fig. 4 show the data with running mean averages applied to the 1-h data in order to highlight the lower-frequency variability in these overviews. The 24-h and 73-h running means remove the diurnal variability in the short-wave radiation and highlight the variability associated with the passage of weather events.

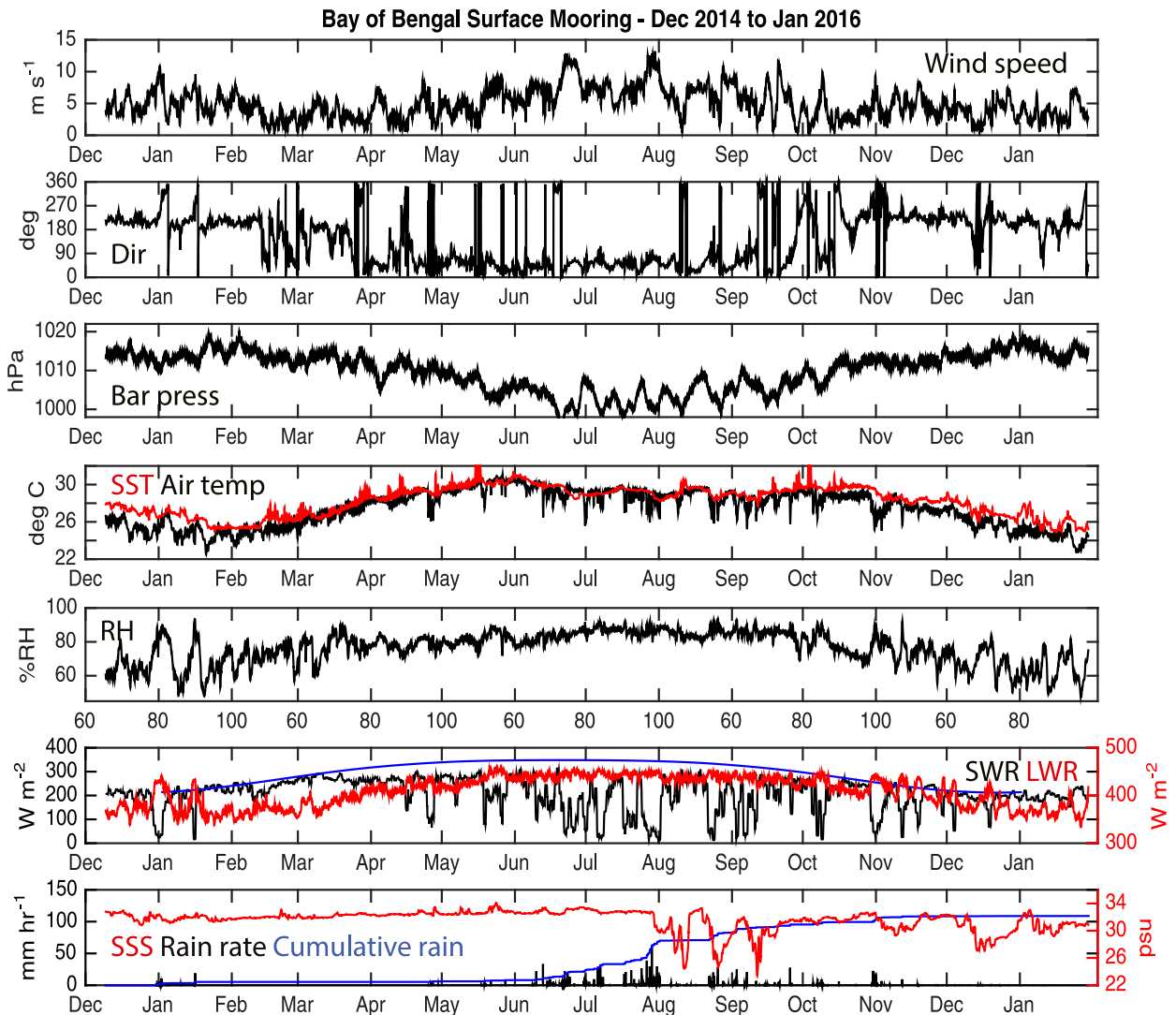An annual cycle was evident in a number of the surface meteorological variables. Wind speed rose in the

FIG. 3. Overview of the surface meteorology at the WHOI mooring. Hourly data were used. (from top to bottom) The variables have running mean averaging indicated in parentheses: wind speed (6 h), wind direction from (6 h), barometric pressure (6 h), air temperature (6 h) in black with sea surface temperature (6 h) in red, relative humidity (6 h), incoming longwave radiation in red (6 h) with incoming shortwave radiation (24 h) in black, and rain rate (no averaging) together with surface salinity (6 h). On the overplot of incoming shortwave and longwave radiation, the blue line shows an estimate of cloud-free or clear-sky shortwave radiation. On the bottom overplot of surface salinity and rain rate, the blue line is the cumulative rainfall in mm scaled by 20 using the left axis, so full scale on the left axis would be 3000 mm or 3 m of rain accumulated.

southwest (SW) monsoon, and wind direction changed from the northeast in the NE monsoon to from the southwest in the summer. The SW monsoon winds were the strongest, with 1-min vector averaged wind speed approaching $20 \, \text{m s}^{-1}$, a maximum hourly averaged wind of $13.5 \, \text{m s}^{-1}$, and SW monsoon season mean of $7.3 \, \text{m s}^{-1}$. Maximum hourly winter winds reached $11.2 \, \text{m s}^{-1}$, and NE monsoon winds from deployment (early December 2014) to the end of February 2015 were $4.5 \, \text{m s}^{-1}$. After the NE monsoon, there was a period of low winds from February to April, including the spring intermonsoon.

The fall intermonsoon had low wind periods but also had more wind events of higher speed than the spring.

Surface barometric pressure was low in the SW monsoon, the season when the relative humidity was highest. Air and sea surface temperatures were higher in the SW monsoon than in the NE monsoon. Winter winds from over the land brought drier, cooler air to the location. Sea surface temperature warmed in the spring intermonsoon and cooled in the fall intermonsoon, but the midsummer sea surface temperatures were cooler than the spring and fall maxima. A striking signal over the year was the
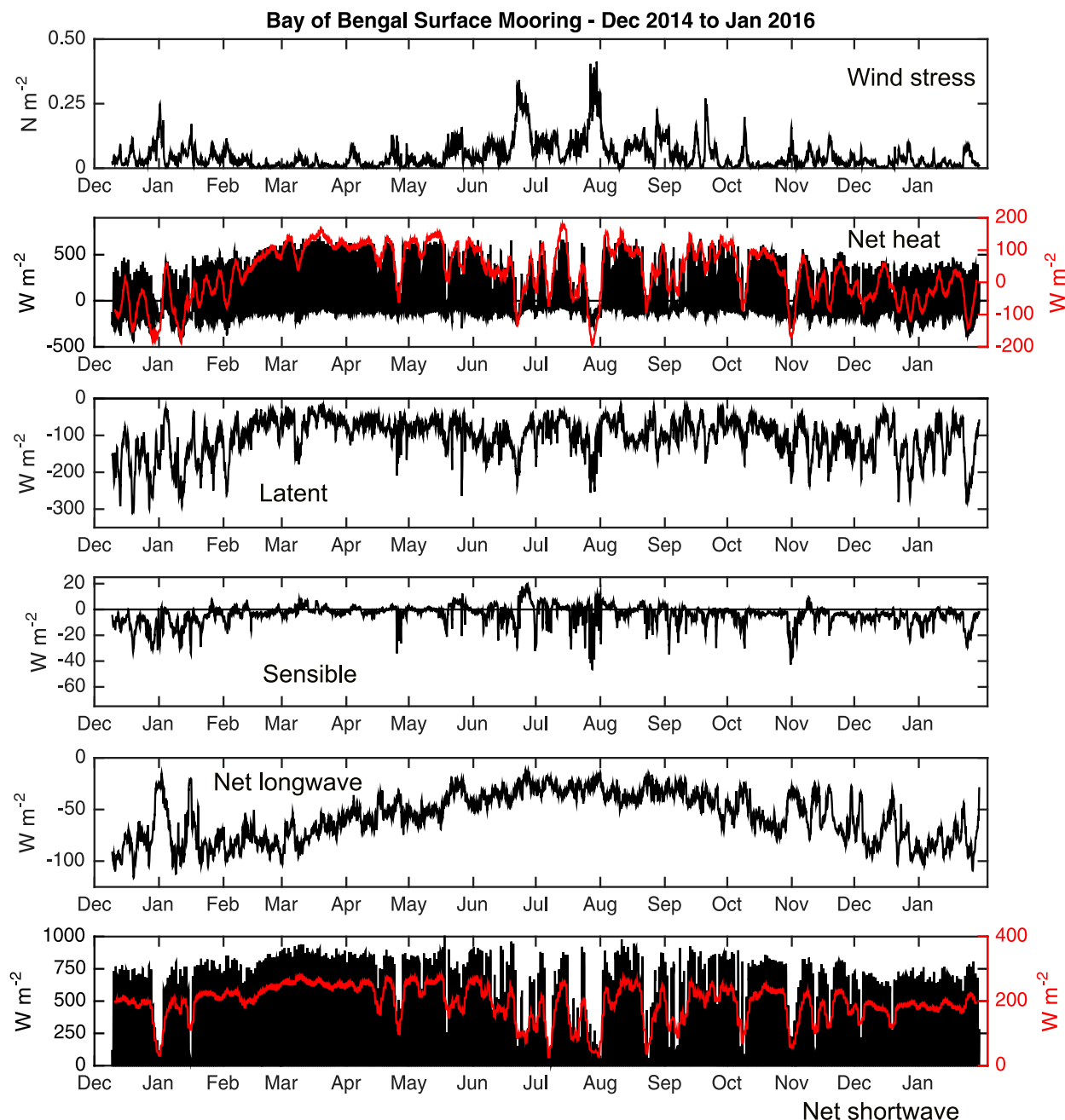
FIG. 4. (from top to bottom) 6-h running mean averages of the 1-h time series: wind stress magnitude, net heat flux (black) together with low-passed (73-h running mean) net heat flux in red, latent heat flux, sensible heat flux, net longwave radiation, and net shortwave radiation with low-passed (73 h) version in red.

change in cloud cover. In Fig. 3 an estimate of the clear-sky incoming shortwave radiation has been plotted with the observed incoming shortwave radiation. The clear-sky radiation is that expected from the sun in the absence of clouds; it captures the daily and annual astronomical variability of insolation at a location, and was calculated from the formulas in the *Smithsonian Meteorological Tables* (List 1984) using an atmospheric transmission

coefficient of 0.72. The clear-sky and observed shortwave are in close agreement during the NE monsoon, pointing to an absence of clouds except during isolated events such as seen at the end of December 2014 into early January 2015. More typically, in the winter, days were clear, and insolation peaked at up to 700–800 W m^{-2}. Only 6% of the observed rainfall came during the NE monsoon. The spring intermonsoon started with clear skies and little

TABLE 1. Full record and year 2015 annual mean values and maximum values from the full record 1-min and 1-h time series of surface meteorology and air–sea fluxes. In the case of variables typically negative, the largest negative values are given. For net heat flux the largest positive and negative values are given.

Variable	Record mean	Annual mean	Hourly maximum	1-min maximum
Wind speed (m s^{-1})	4.9	5.0	14.2	19.7
Wind speed 10 m (m s^{-1})	5.4	5.5	16.0	22.2
Wind direction toward (°)	71.4	56.6	—	—
Air temperature (°C)	27.5	27.8	31.5	31.7
Air temperature 2 m (°C)	27.5	27.8	31.5	31.7
Barometric pressure (hPa)	1009.8	1009.1	1020.9	1021.1
Relative humidity (%)	76.4	78.0	97.6	98.3
Specific humidity (g kg^{-1})	18.7	18.4	24.7	24.9
Specific humidity 2 m (g kg^{-1})	18.9	18.6	24.8	24.9
SST (°C)	28.2	28.5	33.5	34.2
Skin temperature (°C)	28.0	28.5	33.7	34.4
Incoming shortwave (W m^{-2})	204.1	205.8	1068.8	1457.6
Incoming longwave (W m^{-2})	407.8	412.9	468.3	474.7
Rain rate (mm h^{-1})	0.216	0.246	61.6	144.8
Evaporation rate (mm h^{-1})	−0.150	−0.150	−0.502	−0.790
Wind stress magnitude (N m^{-2})	0.054	0.052	0.551	1.265
Net heat flux (W m^{-2})	23.9	36.7	862.7/−479.3	1256.8/−710.0
Latent heat flux (W m^{-2})	−104.6	−101.0	−349.0	−548.8
Sensible heat flux (W m^{-2})	−4.1	−3.4	−99.1	−147.2
Rain heat flux (W m^{-2})	−0.7	−0.8	−244.5	−486.3
Net shortwave flux (W m^{-2})	192.9	194.5	1010.0	1377.5
Net longwave flux (W m^{-2})	−56.9	−53.5	−117.8	−120.6

rain; only 3% of the total precipitation came during the spring. Then, from mid-March to October, observed incoming shortwave was always less than the estimated clear sky value and, at times, much less and close to 0 W m^{-2} in the 24-h averages. Because of the increased summer cloud cover, the spring intermonsoon mean incoming shortwave was the highest and the SW monsoon incoming shortwave was the lowest seasonal mean. Rain accompanied these clouds. The summer monsoon had 65% of the rain, while 24% came during the fall intermonsoon. The total rainfall over the deployment was 2.2 m. The maximum observed rainfall rate in the hourly time series of 61.6 mm h^{-1} came in late July in association with a monsoon depression that developed into cyclonic storm Komen (IMD 2015); the maximum observed 1-min rain rate at this time was 144.8 mm h^{-1}. The seasonal means for net heat flux also reflected the cloud cover variability, and the strongest seasonal mean heating of the ocean, 102.0 W m^{-2}, was during the spring intermonsoon, rather than during the summer monsoon.

Apparent in Fig. 4 is the strong wind forcing of the summer monsoon that accompanied the clouds and rain. The strongest wind forcing events came in July and August during the summer monsoon, with a maximum in 1-h stress of 0.54 N m^{-2} in association with cyclonic storm Komen. During winter, latent heat and longwave net longwave heat loss were both larger. In the heat flux components and the wind stress, events within a season

introduced variability larger than the amplitude of the annual cycle. For example, low-passed (73-h running mean) summer net heat flux (Fig. 4) was negative for a period of days in late July. The increasing cloud cover in the spring followed by the cloudy summer and then decreasing cloud cover in the fall and clear skies of the winter led to an annual cycle in net longwave radiation, cooling the ocean by close to −100 W m^{-2} in the winter but that loss dropping to close to −20 W m^{-2} in the summer monsoon. Similarly, the largest latent heat losses, −342 W m^{-2} in the 73-h average, occurred in the winter monsoon, when the air was drier. Winds were stronger in the SW monsoon but the air–sea humidity gradient was typically less as reported earlier by Bhat (2002); still, moderately large latent heat losses during summer events together with reduction in solar heating due to cloud cover led to generally lower net heat fluxes in the SW monsoon, and the strongest sustained heating occurred during the spring intermonsoon. Rain heat flux is not plotted in Fig. 4; it is plotted later when discussing periods of heavy rain. The maximum hourly rain heat flux of −244.5 W m^{-2} occurred during the passage of Komen as did the maximum in the 1-min rain heat flux of −486.3 W m^{-2}.

Annual means were computed for calendar year 2015 (1 January–31 December 2015). Record means were computed as the average over the 8 December 2014–29 January 2016 deployment. These means are given in Table 1. Table 1 also shows the largest values for each

variable found in the record-long hourly and 1-min time series. In the case of heat flux components and evaporation that are negative, reflecting loss by the ocean, the largest negative values are given, while for net heat flux the largest positive and negative values are given.

The larger values of the 1-min maxima compared to the 1-h maxima reflect the presence of variability on periods shorter than an hour. Higher-frequency variability was evident in several variables: the daily cycle of insolation was accompanied by diurnal warming events seen in surface sea temperature on sunny, low-wind days; downward spikes in air temperature associated with downdrafts from atmospheric convective systems; and the daily variability of the atmospheric tide seen in the barometric pressure. Rotary autospectra of wind velocity and of wind stress (Fig. 5a) showed a small spectral peak around 24 h with more energy in the clockwise component and energy increasing going toward lower frequencies out to about 50 days, a period associated with the intraseasonal oscillations (ISOs). Autospectra of net heat flux (Fig. 5b) showed an energetic spectral peak at 24 h and smaller peaks at harmonics of that frequency.

The time series of wind stress magnitude (Fig. 4) shows wind stress events spaced between 5 and 50 days apart. Intraseasonal variability in the atmosphere in the Bay of Bengal has been noted by Bhat (2002), Vecchi and Harrison (2002), and others. This variability, referred to as intraseasonal oscillations, is associated with the progression of active and break phases of the atmospheric convection. Sengupta et al. (2001) noted coherent, northward propagating, intraseasonal oscillations of satellite-based cloud cover, surface wind speed, net surface heat flux, and sea surface temperature across the Bay of Bengal during the summer monsoon. The amplitude of these events in 2015 was strongest in the summer monsoon, when the wind events were accompanied by dense cloud cover and rain. Wavelet analysis (Fig. 6) and the overview plots (Figs. 3 and 4) pointed to a seasonal variability in the surface meteorology and surface fluxes, including periods with ISOs. The energetic variability at the 24-h period leads to a peak that dominates in the power spectrum that reflects the whole record, but the wavelet power spectrum shows variability within the record, with the strongest continuous period in the spring intermonsoon and periods of weaker diurnal variability in the SW monsoon, when periods of clouds and less insolation led to lower net heat fluxes and periods of lower energy in the wavelet power spectrum. Figure 6d quantifies the lower-frequency variability in the periods of 5 to 50 days, which was most energetic in the

SW monsoon, least energetic in the spring intermonsoon, and had periods of increased variance in the winter monsoon and fall intermonsoon. This seasonal variability is discussed in more detail in the next section.

4. Surface meteorology and air–sea fluxes during the four seasons

Table 2 summarizes the surface meteorological means from the four seasons, and Table 3 summarizes the surface flux means. In this case, winter monsoon means have been computed two ways, averaging from deployment in mid-December 2014 to the end of February 2015 and also as the mean of January 2015, February 2015, and December 2015 in order to capture the full month of December. Spring intermonsoon means are from March, April, and May 2015. The summer or SW monsoon means are from June, July, and August 2015. Fall intermonsoon means are from September, October, and November 2015. Rain heat flux is included in Tables 1 and 3; the SW monsoon had the largest seasonal mean of $-1.7\,\mathrm{W\,m^{-2}}$, close to that season's mean sensible heat flux. The bulk formulas used to compute the fluxes allows flux-dependent extrapolation of air temperature and humidity from observed heights to the model standard height of 2 m and of wind stress to the model standard height of 10 m; these are included in Tables 2 and 3.

a. Winter or NE monsoon

The winter monsoon season showed a transition from dry air from the northeast to moist air from the southwest. Accompanying this change was the change from sustained net heat loss early to the sustained heat gain seen late in the season. The early heat loss in the season is larger and this season mean is the only season of mean net heat loss. The drier air of early winter, including the record minimum of 46.2% RH in hourly data (Fig. 7), in the presence of moderate winds led to the largest seasonal latent heat loss ($-138.4\,\mathrm{W\,m^{-2}}$) and net longwave loss ($-79.0\,\mathrm{W\,m^{-2}}$), contributing to the net heat loss of $-31.9\,\mathrm{W\,m^{-2}}$. Maximum hourly winter monsoon season winds reached $11.2\,\mathrm{m\,s^{-1}}$ but the season mean was $4.5\,\mathrm{m\,s^{-1}}$. Periodic increases in wind speed in January and February associated with the winter ISO variability had corresponding increases in latent heat flux. Most often the skies were clear, but these increases in latent heat flux resulted in the low-passed (73-h running mean) net heat flux remaining negative for several days during such events. One event with particularly heavy cloud cover, some rain, and the strongest winter winds occurred at the end of December and beginning of January (Fig. 8) also yielded a period of oceanic heat loss. Toward the end of the winter monsoon season
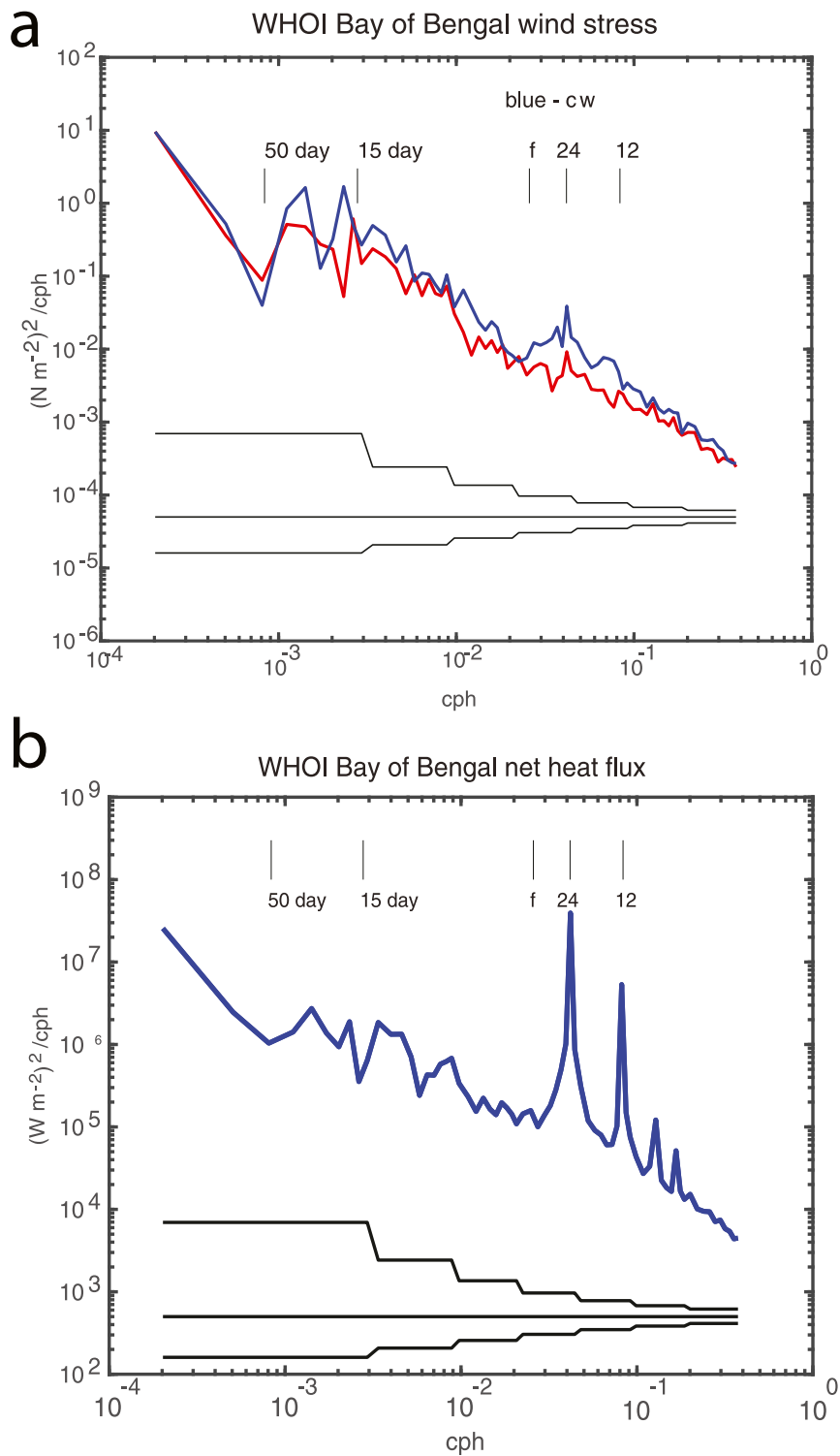
FIG. 5. (a) Rotary autospectrum of wind stress with 95% confidence limits. Clockwise component in blue; counterclockwise in red. Band-averaging increases with frequency. (b) Autospectrum of net heat flux with 95% confidence limits.
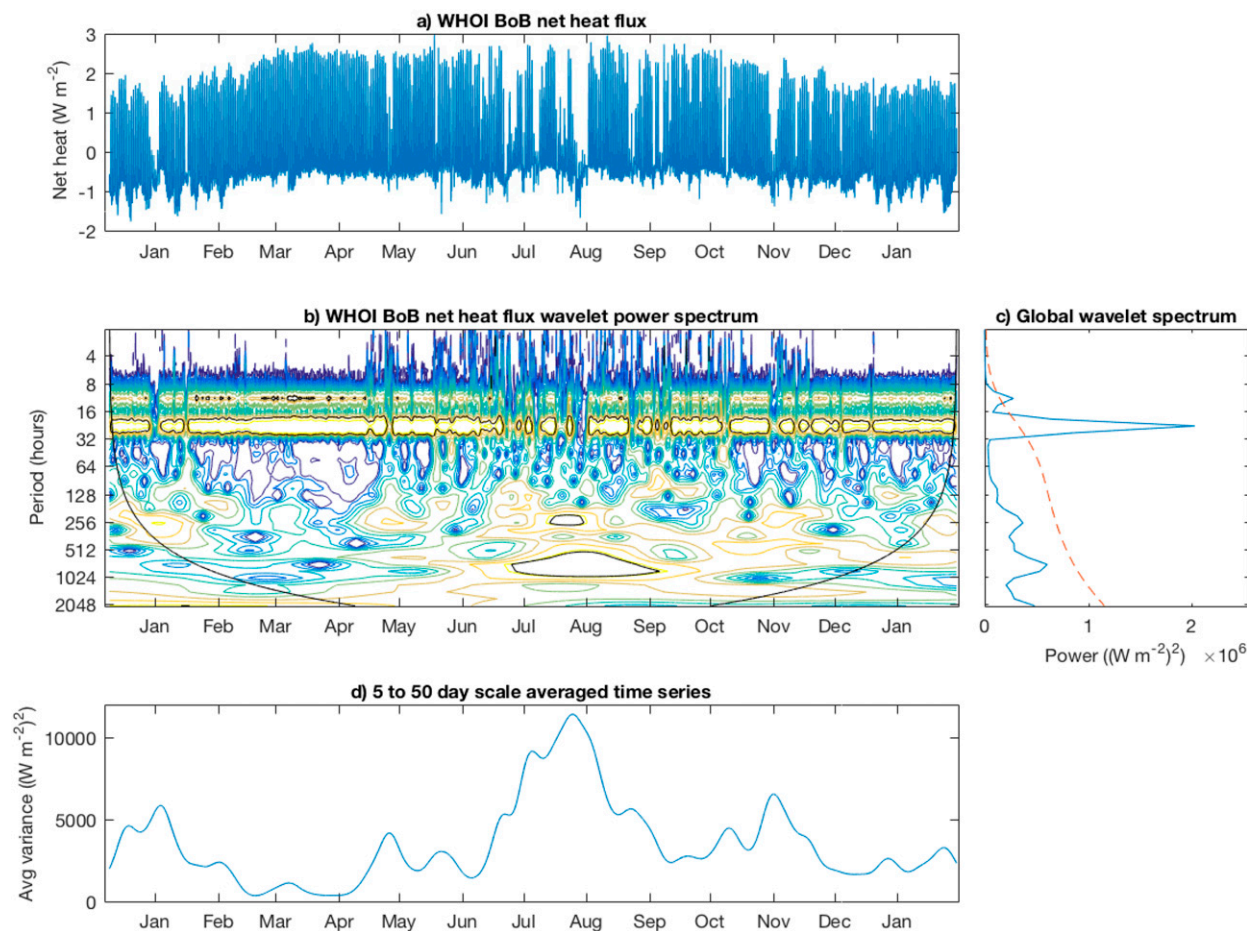
FIG. 6. Wavelet analysis of observed net heat flux time series after Torrence and Compo (1998). (a) The hourly time series of net heat flux plotted vs yearday 2014. (b) The wavelet power spectrum of net heat flux, with interior black contour lines showing the 95% confidence level, and curved lines to the left and right showing the boundaries below which results should be ignored. (c) The power spectrum of net heat flux, with the 95% significance level as the dashed red line. (d) The time variability of the amplitude of the 5 to 50-day portion of the time series.

there was no rain and skies were clear. Wind speed decreased, and wind direction transitioned to toward the north-northeast. Low-passed net heat flux persisted as positive from early February through the end of the season.

The event in Fig. 8 may be atypical of winter in the northern Bay of Bengal. From 29 December to 3 January, a deep depression that developed in the equatorial Indian Ocean on 26 December followed an unusual track to the northern Bay of Bengal and was accompanied by clouds, moist air, and rain. Latent and longwave heat loss were reduced; however, the clouds greatly reduced solar insolation, and daily maxima in net shortwave fell to less than 50 W m^{-2} for three days in a row. Thus, the moist convective event sustained the mean net heat loss seen earlier in the dry and clear conditions. The low-wind, clear-sky conditions immediately following the event gave rise to two days of mean net oceanic heat gain and

were typical of the period of sustained mean oceanic heat gain observed from mid-January until the end of the season.

b. Spring intermonsoon

In the spring intermonsoon season the wind events had low amplitude and cloud cover was infrequent (Fig. 9), so the season typically had a positive low-passed surface heat flux and the highest seasonal mean heating (Table 3). The exception was an event in late April (Fig. 10). The spring intermonsoon mean incoming shortwave was the highest of the four seasons. One consequence of strong solar heating under low winds was diurnal variability observed in both air temperature and sea surface temperature. The air temperature signal was due to solar heating of the air temperature sensor. This sensor was enclosed in a multiplate radiation shield to reduce solar heating of the sensor; however, ventilation of the sensor

TABLE 2. Seasonal means of the surface meteorology. The winter monsoon column with an asterisk is computed from deployment in mid-December 2014 to the end of February 2015. The winter monsoon column without an asterisk is computed using January and February 2015 together with December 2015.

Variable	Winter monsoon (DJF)*	Winter monsoon (DJF)	Spring intermonsoon (MAM)	Summer monsoon (JJA)	Fall intermonsoon (SON)
Wind speed ($m\,s^{-1}$)	4.5	4.1	4.1	7.3	4.5
East wind ($m\,s^{-1}$)	−1.8	−1.6	2.0	4.6	−0.4
North wind ($m\,s^{-1}$)	−3.1	−2.6	1.2	4.6	−0.1
Wind direction (° toward)	210.1	211.6	59.0	45.0	256.0
Air temp (°C)	25.1	25.3	28.5	29.0	28.2
SST (°C)	26.5	26.5	28.9	29.3	29.1
Relative humidity (%)	68.8	69.0	79.2	84.9	78.8
Spec humidity ($g\,kg^{-1}$)	13.7	13.9	19.4	21.5	18.9
Shortwave ($W\,m^{-2}$)	204.8	202.8	250.0	176.5	194.6
Longwave ($W\,m^{-2}$)	373.5	375.4	413.0	440.7	421.3
Conductivity ($S\,m^{-1}$)	5.03	4.93	5.35	5.26	5.17
Salinity (psu)	31.94	31.19	32.46	31.60	31.09
Sigma ($kg\,m^{-3}$)	20.59	20.02	20.19	19.40	19.09
Precipitation rate ($mm\,h^{-1}$)	0.05	0.04	0.03	0.68	0.23
Bar pressure (hPa)	1013.9	1014.2	1009.7	1003.1	1009.6

inside the shield was passive, and in low wind during the day the sensor reads too warm. Anderson and Baumgartner (1998) found this heating during winds under ~3 m s⁻¹, increasing as wind speed decreased. Thus, the series of larger positive excursions in air temperature midday on 8 to 16 April (Fig. 10) during the low winds are considered to include error due to radiative heating of the sensor shield and enclosed air. In contrast to these air temperature increases, the increases in sea surface temperature are considered to correctly capture heating of the near-surface ocean by the solar radiation. These diurnal warming events have been studied by Prytherch et al. (2013), Weller et al. (2014), and others. Another short-lived excursion in air temperature is the downward spikes, as seen on 25–28

April 2015 (Fig. 10). Such events were seen in association with clouds and rain and are attributed to cool air descending as part of the structure of mesoscale convective systems (Houze 2004).

Few such convective systems were observed in the spring intermonsoon; clear skies, with ongoing sustained oceanic heat gain, characterized the season. The change in direction of the wind toward the end of the winter monsoon season replaced dry air with moist, and the spring intermonsoon mean latent heat loss of −77.4 W m⁻² was the least of all the seasons. The sensible heat loss of −0.7 W m⁻² was also the least of any season. In contrast, the mean net shortwave gain of 236.3 W m⁻² was the largest of all the seasons. As a result, the spring intermonsoon mean net heat gain by the ocean of 102.0 W m⁻² was the

TABLE 3. Seasonal means of the surface fluxes. The winter monsoon column with an asterisk is computed from deployment in mid-December 2014 to the end of February 2015. The winter monsoon column without an asterisk is computed using January and February 2015 together with December 2015. The bulk algorithm extrapolates air temperature and humidity to 2 m and wind speed to 10 m.

| Variable	Winter monsoon (DJF)*	Winter monsoon (DJF)	Spring intermonsoon (MAM)	Summer monsoon (JJA)	Fall intermonsoon (SON)
Sensible ($W\,m^{-2}$)	−8.0	−6.1	−0.7	−1.6	−5.2
Latent ($W\,m^{-2}$)	−138.4	−123.1	−77.4	−102.0	−101.2
Net longwave ($W\,m^{-2}$)	−79.0	−77.2	−56.2	−32.2	−49.2
Net shortwave ($W\,m^{-2}$)	193.6	191.6	236.3	166.8	183.9
Net heat ($W\,m^{-2}$)	−31.9	−14.7	102.0	31.0	28.4
Rain heat flux ($W\,m^{-2}$)	−0.0	−0.0	−0.0	−1.7	−0.2
Stress magnitude ($N\,m^{-2}$)	0.043	0.035	0.032	0.108	0.042
Stress direction (° toward)	214.6	216.0	51.3	49.3	355.8
East stress ($N\,m^{-2}$)	−0.020	−0.016	0.015	0.079	−0.000
North stress ($N\,m^{-2}$)	−0.029	−0.022	0.012	0.068	0.004
2-m air temperature (°C)	25.2	25.4	28.5	29/1	28.2
2-m specific humidity ($g\,kg^{-1}$)	13.9	14.0	19.5	21.6	19.0
10-m wind speed ($m\,s^{-1}$)	5.0	4.5	4.4	8.1	4.9
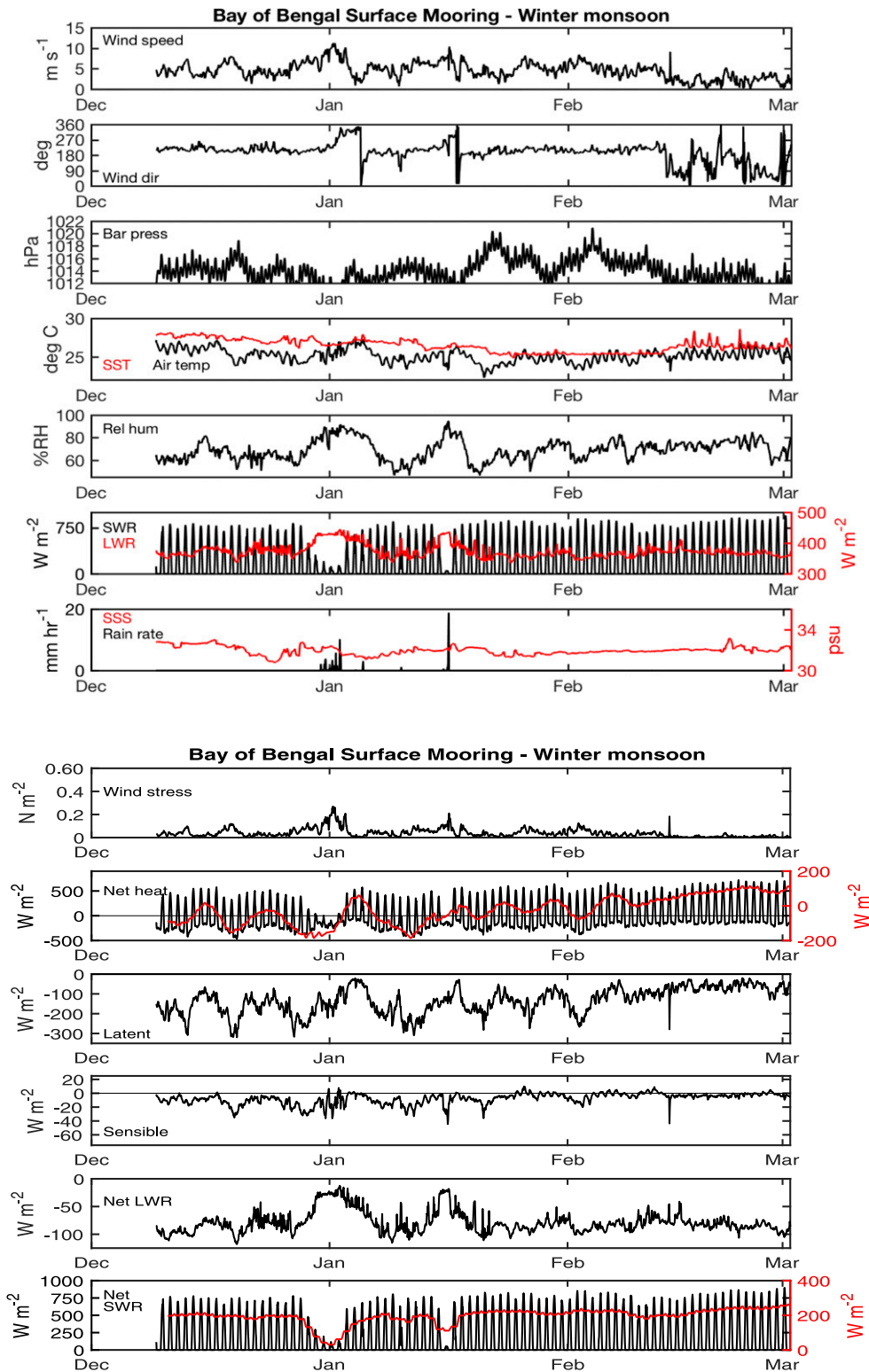
FIG. 7. (top) Hourly surface meteorology during winter. Sea surface temperature (SST), incoming longwave radiation (LWR), and sea surface salinity (SSS) are red in the overplots. Incoming shortwave radiation is labeled SWR. Wind direction is direction toward. (bottom) Hourly wind stress magnitude and heat fluxes. Hourly net heat flux and net shortwave radiation are shown hourly in black and with a 73-h running mean in red.
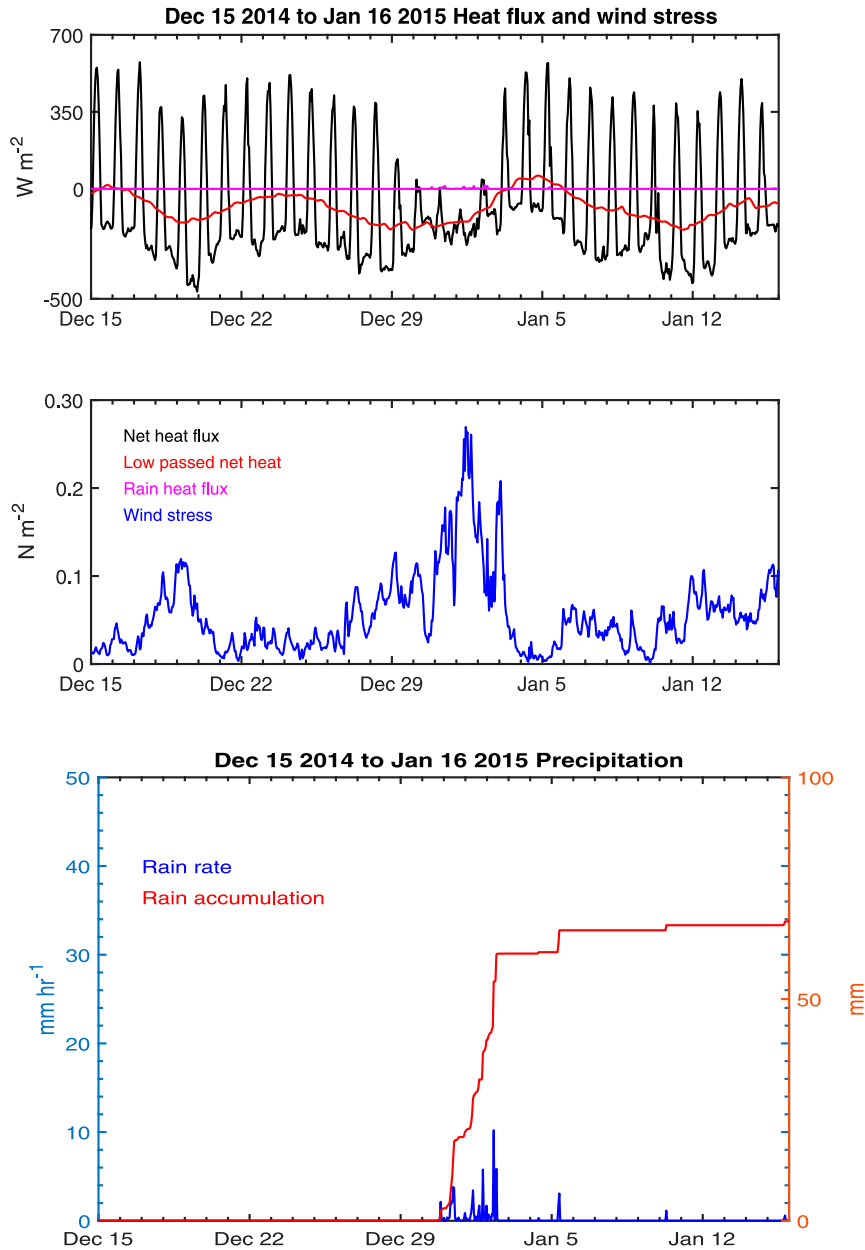
FIG. 8. For 15 Dec 2014 to 16 Jan 2015 (top) hourly net heat flux (black), rain heat flux (magenta), and 73-h running mean of net heat flux (red), with (middle) hourly wind stress (blue) and (bottom) hourly rain rate (blue) and accumulated rain (red).

largest of all the seasons, driven by the regime of clear skies, strong solar heating, low wind speeds of moist air, and infrequent mesoscale convective events in the atmosphere.

c. Summer or SW monsoon

The strongest wind forcing events came in July and August during the summer monsoon season with a maximum in 1-h stress of $0.55 \, \mathrm{N \, m^{-2}}$. The summer monsoon winds were the strongest, with 1-min vector averaged wind speed approaching $20 \, \mathrm{m \, s^{-1}}$, a maximum

hourly averaged wind of $14.2 \, \mathrm{m \, s^{-1}}$, and a summer season mean of $7.3 \, \mathrm{m \, s^{-1}}$ (Fig. 11). Although the event in late July to early August follows a period of increased wind stress in the latter half of June by about 40 days, suggestive of the periodicity of the ISOs, the second event has been identified as the passage of Tropical Cyclone Komen and is shown in more detail in Fig. 12. Komen was the fourth system during July that intensified into a cyclonic storm in the Bay of Bengal since 1965 and is described by the Indian Meteorological
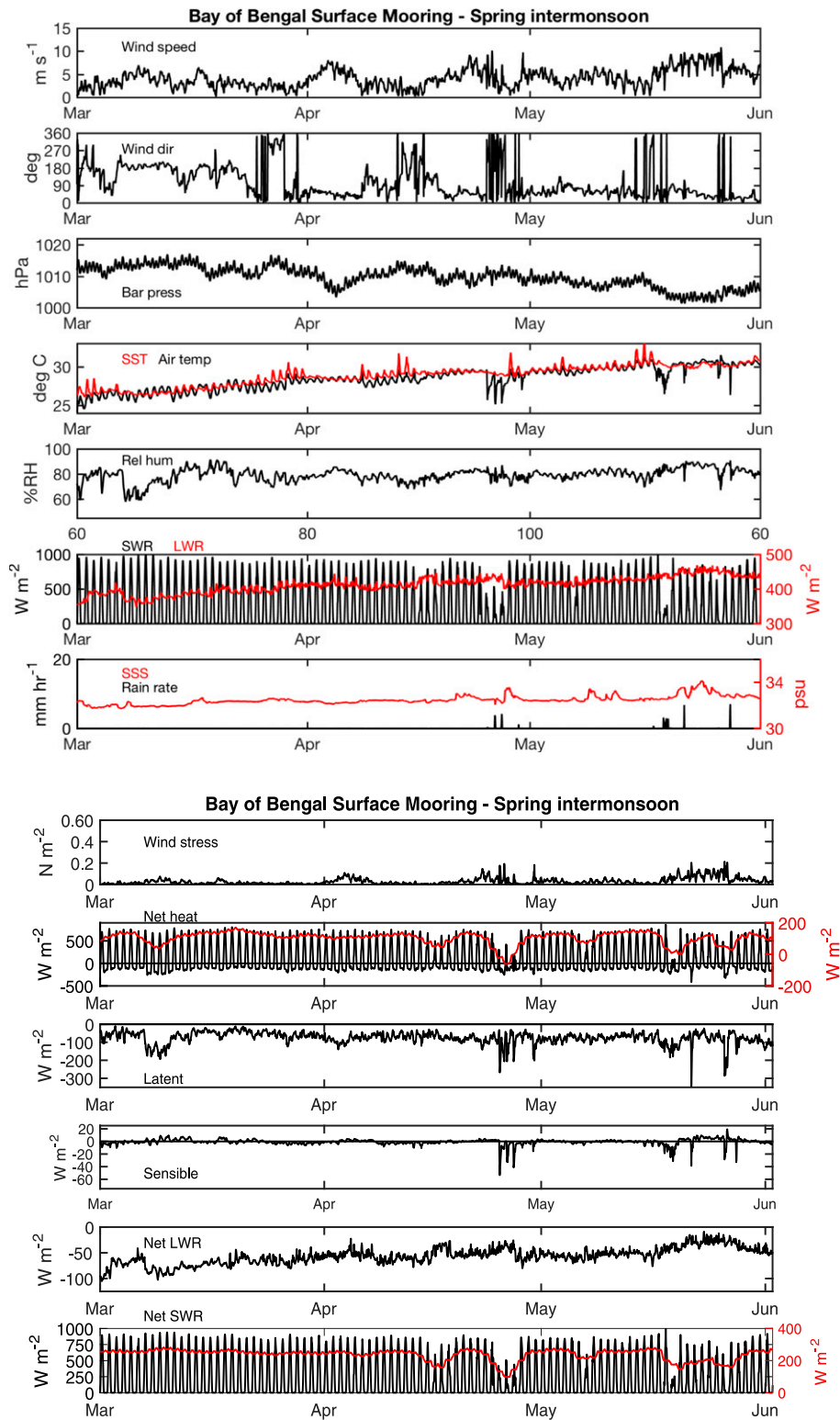
FIG. 9. (top) Hourly surface meteorology during the spring intermonsoon season. SST, incoming LWR, and SSS are red in the overplots. Wind direction is direction toward. (bottom) Hourly wind stress magnitude and heat fluxes. Hourly net heat flux and net shortwave are shown in black and with a 73-h running mean in red.
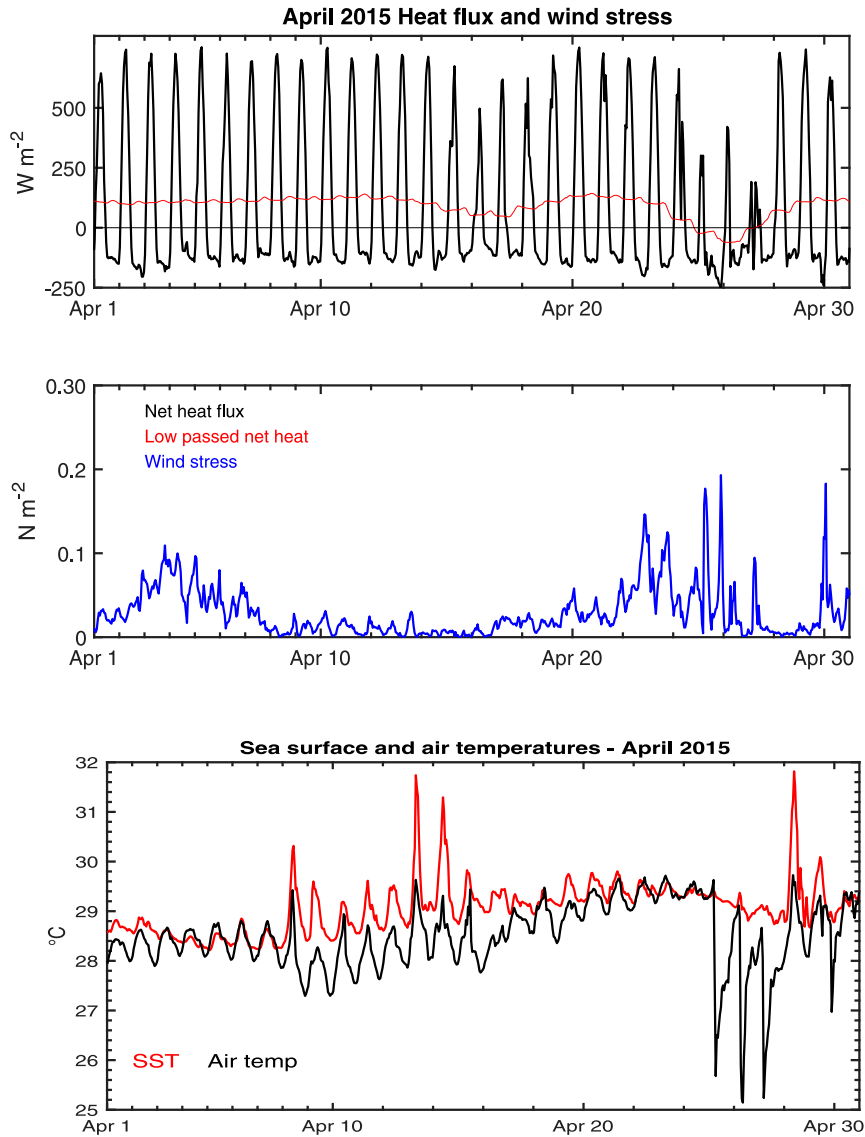
FIG. 10. (top) The hourly net heat flux (black) and 73-h running mean net heat flux (red) during the month of April 2015. (middle) Hourly wind stress magnitude and (bottom) an overplot of hourly sea surface temperature (SST) (red) and air temperature (black).

Department preliminary report on Komen (IMD 2015) issued in August 2015. Komen had a circular track moving counterclockwise through the northern Bay of Bengal and onto land, with a closest approach to the buoy just north of 21°N on 29 July 2015. The strongest recorded winds at the buoy occurred at this time. INSAT-3D visible imagery in that report show the large pattern of cloud cover associated with Komen responsible for very low levels of daily mean net shortwave radiation in the last week of July (Fig. 12), and TRMM 0.25° spatial resolution maps of daily rainfall show a large area of heavy rain over the northern Bay of Bengal and the mooring during that week with daily rain

rates of up to $100 \, \mathrm{mm \, day}^{-1}$, corresponding well to the 700 mm total seen at the buoy for that week. Although Komen shows as a large-scale feature across the northern Bay of Bengal in the satellite data, the cold air spikes and short-lived periods of heavy rain illustrated in Fig. 12 show that the cyclone had convective features at smaller scales that were sampled by the buoy as the cyclone moved past.

During Komen a negative net heat flux persisted at the sea surface due to greatly reduced insolation combined with higher latent heat flux (Fig. 12). Maximum hourly net shortwave radiation for the day of 1 August 2015 was only $25.2 \, \mathrm{W \, m}^{-2}$. The late July to early August event contributed 0.70 m of rain, and a peak hourly rain rate of
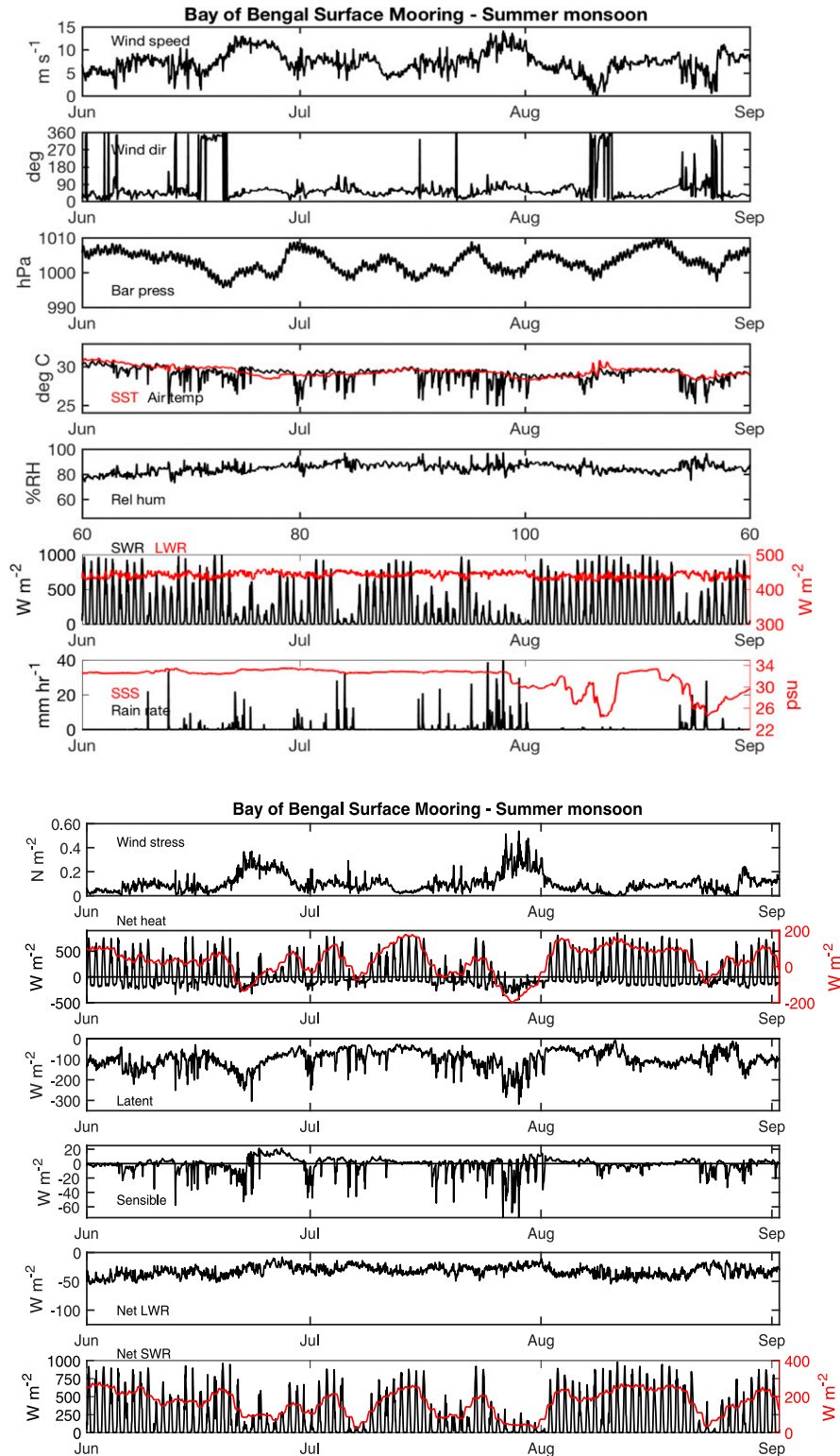
FIG. 11. (top) Hourly surface meteorology during the summer monsoon. SST, incoming LWR, and SSS are in red in the overplots. Wind direction is direction toward. (bottom) Hourly wind stress magnitude and heat fluxes. Net heat flux and net shortwave radiation (SWR) are shown hourly in black and with a 73-h running mean in red.
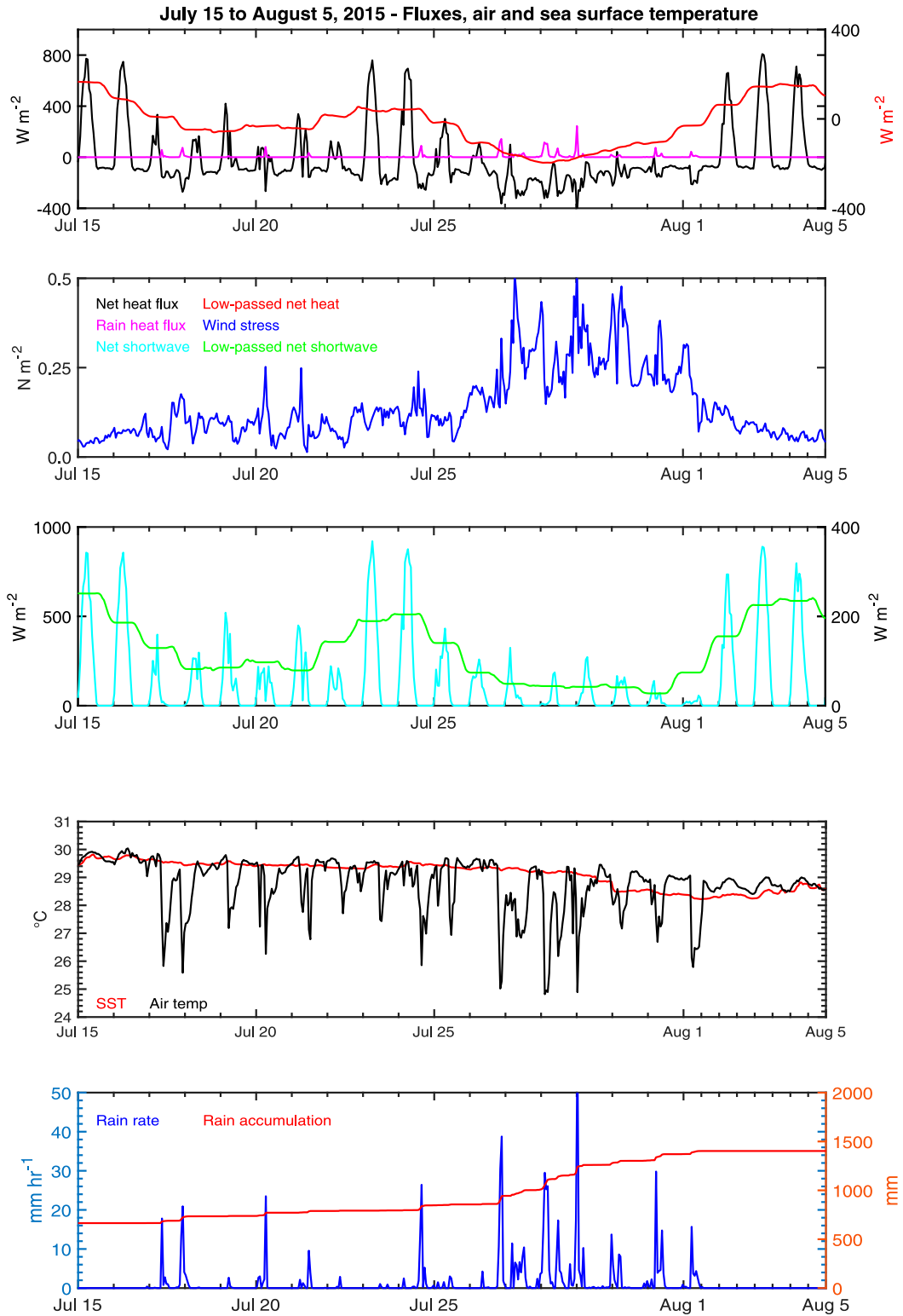
FIG. 12. Hourly time series from 21 days of the summer, 15 Jul to 5 Aug 2015. At the top are shown hourly net heat flux (black), 73-h low-passed net heat flux (red), and hourly rain heat flux (magenta). Directly below, hourly wind stress magnitude, then hourly net shortwave radiation (cyan) and 73-h low-passed shortwave radiation (green) below that. Second from bottom, hourly air temperature (black) and sea surface temperature (SST) (red). At the bottom, hourly rain rate (blue) and rain accumulation (red).

$61.6\,\mathrm{mm\,h^{-1}}$ and peak 1-min rain rate of $144.8\,\mathrm{mm\,h^{-1}}$ were associated with this event. The cool downdrafts and outflow dropped hourly air temperature briefly by over 4°C and brought the hourly wind speed maximum up to $14.2\,\mathrm{m\,s^{-1}}$. The lowest low-passed net heat flux during this period reached close to $-196\,\mathrm{W\,m^{-2}}$ and the lowest hourly net heat flux was $-441.6\,\mathrm{W\,m^{-2}}$. This lowest hourly net heat flux was associated with a short-lived event early on 30 July, when high winds, heavy rain, and a 4°C drop in air temperature coincided. The $-441.6\,\mathrm{W\,m^{-2}}$ hourly net heat flux was due mainly to an hourly latent heat flux of $-318.4\,\mathrm{W\,m^{-2}}$ and an hourly sensible heat flux of $-98.1\,\mathrm{W\,m^{-2}}$. The hourly rain heat flux, not included in this net heat flux value, was significant at $-244.5\,\mathrm{W\,m^{-2}}$; it is plotted in Fig. 12.

In addition to Komen, the amplitude of the ISO events in 2015 was strongest in the SW monsoon season, when the wind events were accompanied by dense cloud cover and rain. The stronger ISOs of the summer monsoon resulted in modulation of the net heat flux, with periods of surface cooling associated with strong wind forcing, reduced insolation, and increased latent heat flux. Six periods of reduced net heating were evident (Fig. 11), and the summer monsoon seasonal mean net heat flux of $31.0\,\mathrm{W\,m^{-2}}$ is much smaller than that of $102.0\,\mathrm{W\,m^{-2}}$ in the spring.

d. Fall intermonsoon

The fall intermonsoon season was transitional, with moderate wind events and periods of cloud cover that reduced insolation (Fig. 13). The wind direction reversed first for several days at the end of September and into early October before going back toward the north-northeast for a week in October. During mid-October and onward through fall the flow was toward the south-southeast. As the moist air of the early fall intermonsoon was replaced by drier air off the land there was an accompanying increase in latent heat loss. Net longwave heat loss also increased through the season. However, skies were most often clear. Because of less cloud cover, even though the summer solstice was passed, the fall intermonsoon mean net shortwave radiation of $183.9\,\mathrm{W\,m^{-2}}$ was close to $20\,\mathrm{W\,m^{-2}}$ higher than the summer monsoon season mean. As in the summer monsoon season, a few events with wind, rain, cloud cover, and cooler air temperatures were seen; and low-passed net heat flux did during these events become negative. However, the fall intermonsoon season mean net heat flux reflected an average oceanic gain of $28.4\,\mathrm{W\,m^{-2}}$, close to the summer monsoon season mean gain of $31.0\,\mathrm{W\,m^{-2}}$.

5. Discussion

The 14-month record from the surface mooring spanned an annual cycle and captured the variability across the seasons, including the summer and winter monsoons.

Motivation for collecting the observations had included improving an understanding of the role of local air–sea interaction in the evolution of the upper ocean in the northern Bay of Bengal. The overview of the observations (Fig. 3) had also illustrated how sea surface temperature (SST) and sea surface salinity (SSS) evolved over the record. SST showed tracked closely with air temperature, with trends varying over the seasons. SSS increased slowly until August, when a series of lower-salinity events marked the end of the summer monsoon and early fall intermonsoon. The last phase of this analysis sought to answer these questions: To what extent is the observed surface forcing capable of contributing to the evolution of SST and SSS? Are the different seasons in the northern Bay of Bengal potentially characterized by different regimes of local air–sea interaction?

As discussed above, the surface meteorology and fluxes differed between the seasons. Figure 14 provides a summary from the perspective of the accumulated air–sea freshwater flux, accumulated air–sea heat, and time integral of the wind stress. The integrated quantities are computed to highlight differences between seasons and periods during the year when major contributions occurred as indicated by the steeper slopes. In the case of the integral of the stress, the steeper slopes highlight periods of potential wind-driven mixing stronger wind-driven transport and the curve provides a means to contrast cumulative mechanical forcing in the different seasons. Freshwater flux varied seasonally due to rainfall. The winter monsoon had stronger evaporation, but Fig. 14 shows that evaporation was ongoing, and evaporation dominated precipitation from December 2014 through the end of July 2015. Freshwater accumulated (Fig. 14) from late July through early November, with close to 1 m added. From November onward, evaporation again dominated. The major wind stress events coincided with the rain events in the summer monsoon. Heat loss marked December 2014 through January 2015 and again in December 2015 through January 2016. Toward the end of winter there is an inflection point in the integrated heating (Fig. 14) as the low-passed net heat flux became positive under clear skies and increasing insolation. The spring intermonsoon exhibited the strongest sustained heating of the ocean, which is reflected by the maximum positive slope of the accumulated heating in Fig. 14. During the summer monsoon the integrated heating curve is flat much of the season (Fig. 14). Two months of sustained heating marked the beginning of the fall intermonsoon. A return of drier air from the northeast and increased net longwave loss together with seasonal decrease in insolation are reflected by in inflection point and return to a negative slope in the time integrated heating. Figure 14 was made without
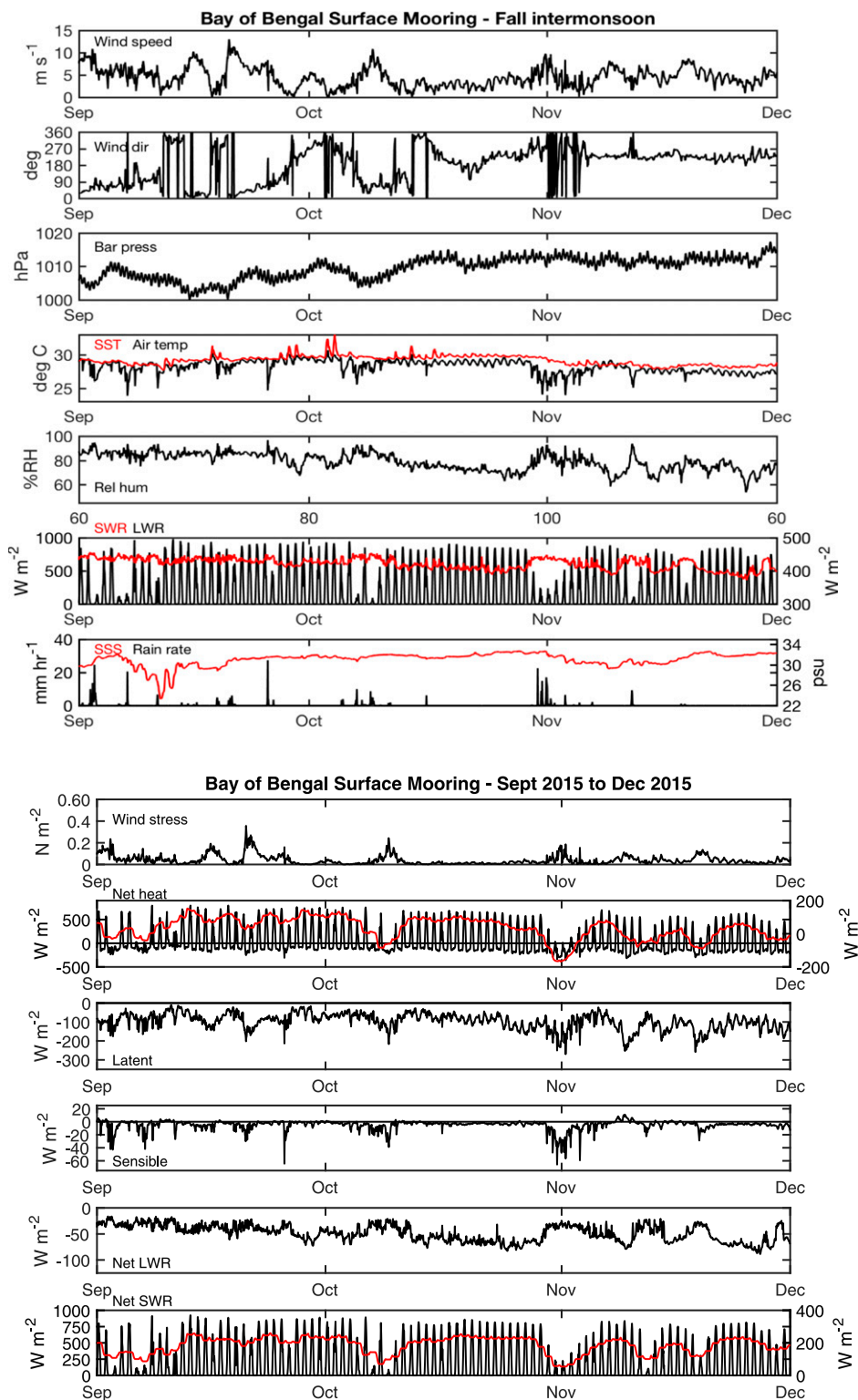
FIG. 13. (top) Hourly surface meteorology during the fall intermonsoon. SST, incoming LWR, and SSS are red in the overplots. Wind direction is direction toward. (bottom) Hourly wind stress magnitude and heat fluxes. Net heat flux and net SWR are shown hourly in black and with a 73-h running mean in red.
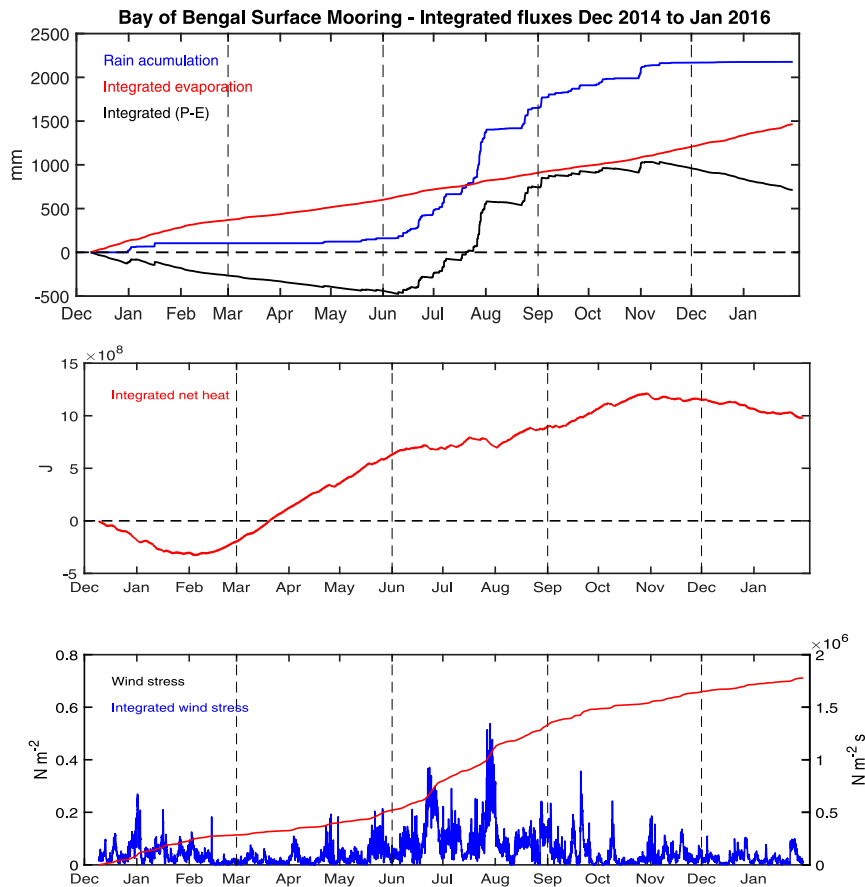
FIG. 14. (top) Time-integrated freshwater flux, showing the accumulated rainfall, the accumulated evaporation (taken as positive), and the total freshwater accumulation (accumulated precipitation minus accumulated evaporation). (middle) Time integral of the surface net heat flux. (bottom) Hourly wind stress magnitude as well as the time integral of the wind stress magnitude. The boundaries of the four seasons discussed in the text are indicated by dotted vertical lines.

inclusion of the rain heat flux. Including the rain heat flux lowers the final value of the heat accumulation by 2.5% and does not noticeably change the heat accumulation curve.

The observed freshwater and heat flux were applied to a simple model of the ocean surface layer and the resulting evolution of surface temperature and salinity contrasted to those observed. Oceanographic instrumentation on the mooring allowed us to compute the depth of the surface mixed layer following Lorbacher et al. (2006). That mixed layer depth (Fig. 15) was used at hourly time resolution, except where the calculation yielded small mixed layer depth values including some zeroes, in which case depths less than a chosen minimum were set to that minimum. The observed low-passed (72 h) mixed layer (Fig. 15) deepened to close to 50 m during the winter; became shallow, around 10 m, in the spring; deepened in the summer in response to the strong wind events; and shoaled in August to remain shallow, around 5–15 m through the end of the record.

Other studies, such as Sengupta et al. (2006), have pointed to the inflow into the northern Bay of Bengal by five of the largest rivers. Sengupta et al. (2006) show a seasonal cycle in the freshwater terms with a peak in runoff into the Bay of Bengal in mid-August and a peak in precipitation that comes earlier, in June. The question addressed here is this: How would the observed local freshwater surface flux, evaporation and precipitation change the salinity of the observed mixed layer in the absence of advection? Evaporation was computed from the latent heat flux and combined with the observed precipitation to obtain the freshwater flux (Fig. 15). The evolution of surface layer salinity using a mixed layer depth minimum of both 3 m and 10 m is shown in Fig. 15 compared to the observed surface salinity, which came from 1-m depth. The trend through midsummer of slowly increasing surface layer salinity was replicated in both cases, suggesting that surface salinity increased under the influence of evaporation. In the summer, rain events dropped the predicted salinity of the
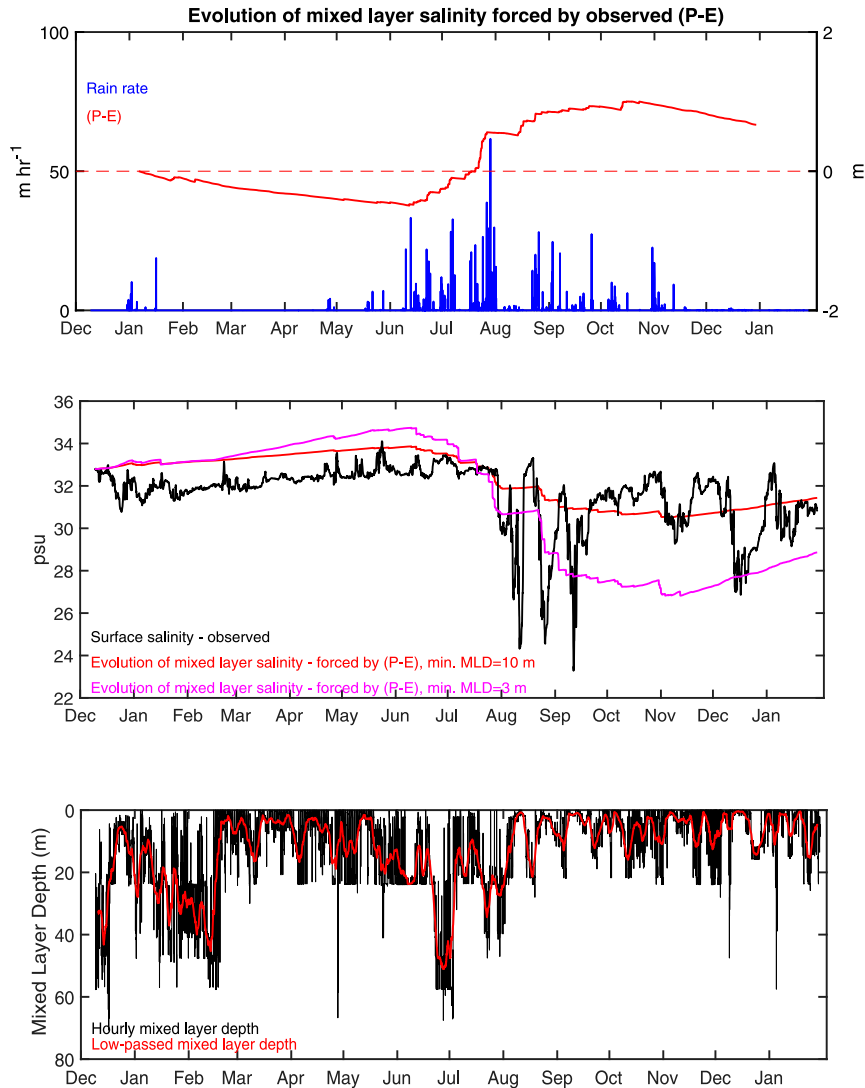
FIG. 15. (top) Hourly rain rate and cumulative precipitation minus evaporation ($P - E$) as in Fig. 14. (middle) Comparison of the observed sea surface salinity with the evolution of the surface layer salinity in response to observed freshwater flux and mixed layer depth, for two cases, with minimum mixed layer depth set to 3 m and minimum mixed layer depth set to 10 m. (bottom) Hourly observed mixed layer depth and 72-h low-passed mixed layer depth.

surface in late July and again in late August. These predicted drops line up with observed decreases in salinity but were not as fresh or as short-lived as the observed salinity signals. Other sharp drops in observed salinity in mid-August and mid-September were not matched by drops in predicted salinity.

The simple model distributes the surface freshwater flux through the mixed layer, and shallow mixed layers respond with proportionately larger change in salinity. Figure 15 shows the mixed layer deepening to ~60 m at the time of the first rain and wind event of the summer monsoon in late June. The second, stronger wind and rain event of later July to early August, however, was

accompanied by two short-lived excursions of the mixed layer to 40 m and followed mixed layers in August and the early fall intermonsoon that were very shallow, often less than 5 m. The shallow mixed layers of August and September are thus responsive to additions of freshwater. This is further illustrated by the case in which the minimum mixed layer depth is set to 3 m in the model and the predicted salinity drops 6 psu across the summer monsoon. The model may, by enforcing a limit to the minimum value, may have underestimated the potential magnitude of the freshening accompanying the rain events by applying the rain to a deeper than observed mixed layer. The model has no representation of riverine

influxes of lower-salinity water. However, the computation does support evaporation as capable of explaining trends of increasing surface salinity during the intermonsoons and the potential for heavy rainfalls in the summer monsoon to drop surface salinity significantly at a time earlier than the August peak in the river runoff.

The surface heat flux was applied to the surface layer and the evolution of surface temperature computed for three cases: first, a mixed layer depth with the minimum set at 10 m and all the penetrating shortwave radiation absorbed within the mixed layer; second, using the same minimum of 10 m and allowing radiation to penetrate the base of the mixed layer using a double exponential formula; and third, using a minimum mixed layer depth of 3 m and allowing penetrating radiation through the base of the mixed layer using the same double exponential formula. In that formula for penetrating radiation, two different sets of parameters were used. Following Paulson and Simpson (1977), 62% of the radiation was taken as red, with an *e*-folding depth of 1.5 m, and 38% as blue-green with an *e*-folding depth of 20 m. In addition, following recent results from ASIRI reported by Lotliker et al. (2016), penetrating solar radiation was computed using 40% of the radiation taken as red with an *e*-folding depth of 0.9 m and 60% as blue-green with an *e*-folding depth of 20.8 m.

Figure 16 summarizes the results. When no penetration of radiation through the mixed layer base was allowed the surface heat flux provided too much heating even when the minimum mixed layer depth was set to 10 m, and the predicted surface temperature warmed steadily from mid-February to late October. Using the Paulson and Simpson (1977) parameterization and setting the mixed layer depth minimum to 10 m yielded an evolution over the seasons of SST that somewhat replicated the observed SST. However, using a shallower minimum mixed layer depth that allowed more heat loss through the base of the mixed layer yielded both warming and cooling trends that were too strong. Using the Lotliker et al. (2016) parameterization that partitions more energy into the blue-green light results in less warming and trends in surface temperature that track those observed through late summer (Fig. 16). From late summer through the end of the record, when the observed mixed layer was shallow, the Lotliker et al. (2016) parameterization resulted in stronger than observed cooling. Thus, while Fig. 16 indicates that the surface heat flux has the potential to contribute significantly to the evolution of surface temperature, it also shows that use of the observed heat flux in a model or in a surface layer heat budget will require care in modeling the penetration of radiation. The large difference in the evolution of estimated SST between the two different parameterizations supports the need for inclusion of

observations of the optical properties of seawater in the northern Bay of Bengal in future studies.

6. Conclusions

The surface mooring deployed for 14 months in the northern Bay of Bengal successfully returned records of surface meteorology and air–sea fluxes. The annual cycle, with a winter NE monsoon, a summer SW monsoon, and spring and fall intermonsoons has been characterized and broken down into four 3-month seasons for further discussion. Within the year, high-frequency variability was associated with the solar insolation and, in the 5- to 50-day range, the variability associated with ISOs was observed. Seasonal differences in wind direction and the humidity of the air, in cloud cover, in the occurrence of ISOs and their accompanying wind, rain, and cloud cover lead to seasonal differences in the air–sea fluxes of heat, freshwater, and momentum. The spring intermonsoon had the strongest mean oceanic heat gain, ongoing evaporation, and little wind forcing. The summer monsoon includes is dominated by strong rains and wind forcing events, with little mean heat gain. The fall intermonsoon was transitional, starting with ISO variability accompanied by heat and freshwater gain and changing to heat and freshwater loss under low winds. The strongest oceanic heat loss accompanied the winter monsoon, a period of evaporation, with little rain and lower winds than the summer monsoon.

The intensity of the surface forcing observed by the buoy was, at times, striking. The maximum observed in the 1-min rain rate was 144.8 mm h^{-1}. Peak 1-min wind speed reached 19.7 m s^{-1}. The largest 1-min net heat flux was 1256.8 W m^{-2}, while the minimum was -710.0 W m^{-2}. Heavy cloud cover accompanying convective systems was able to drop daily mean incoming shortwave radiation to as low as 9.7 W m^{-2}.

Given the intensity of the surface forcing, the seasonally different forcing regimes, and the shallow observed ocean surface layer depths, it was of interest to examine the potential for the surface forcing to be a source of observed variability in surface temperature and salinity.

Application of the observed freshwater and heat flux to simple models of the ocean surface layer did show that the fluxes have the potential to cause significant variability in the upper ocean. The increasing salinity through June can be attributed to evaporation and the initial heavy rains of the summer monsoon summer aligned with observed fresh events in surface salinity. The initial cooling followed by heating through the spring and summer was sufficient to cause trends in surface temperature similar to those observed, although from late fall to winter the trends supported by the surface heat flux do not match those observed. However, attempts to apply
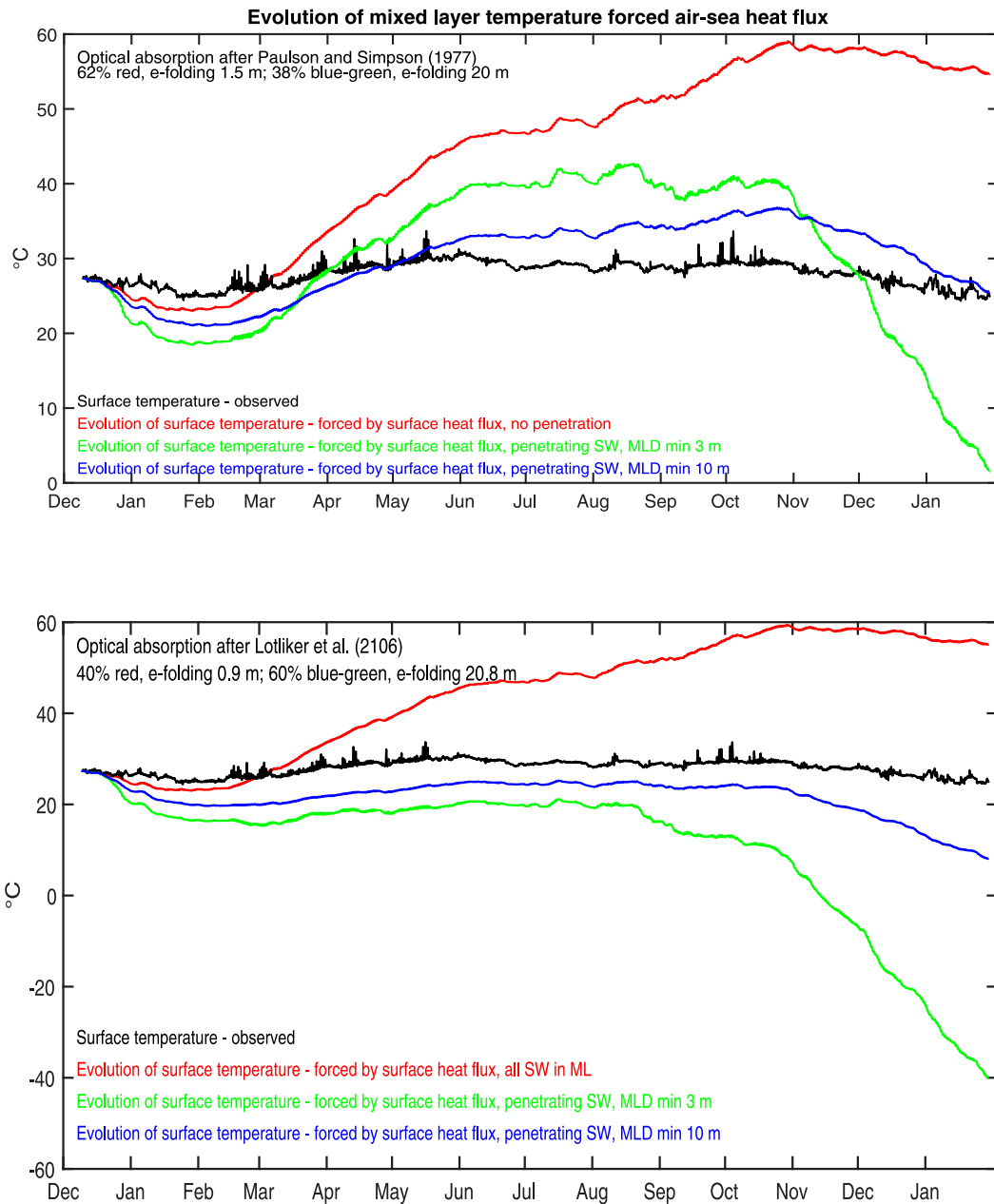
FIG. 16. Mixed layer temperatures computed by applying the surface heat flux to the observed mixed layer depth with the minimum depth set to either 3 m or 10 m compared to observed surface temperature. Two sets of calculations are shown; (top) penetration of the shortwave radiation has been parameterized as in Paulson and Simpson (1977), and (bottom) the shortwave penetration follows Lotliker et al. (2016). In each case the calculation was also done with all the shortwave absorbed within the mixed layer.

observed heat flux to the upper ocean are sensitive to how the penetration of solar radiation is parameterized.

Further efforts to investigate the evolution of the upper ocean in the northern Bay of Bengal should consider riverine inputs as well as ocean advection and mixing. The intent here was illustrate here the rich variability, including intense, short-lived events, seen when the surface meteorology and air–sea fluxes are well resolved in time at a point and, by doing so, to highlight that other representations of the surface forcing that result from averaging in space and/or in time may fail to be realistic in representing the surface forcing. The intent was also to document the buoy time series that are available at http://uop.whoi.edu/projects/Bengal/QCData.html.

REFERENCES

Anderson, S. P., and M. F. Baumgartner, 1998: Radiative heating errors in naturally ventilated air temperature measurements made from buoys. *J. Atmos. Oceanic Technol.*, **15**, 157–173, https://doi.org/10.1175/1520-0426(1998)015<0157:RHEINV>2.0.CO;2.

Bhat, G. S., 2002: Near-surface variations and surface fluxes over the northern Bay of Bengal during the 1999 Indian summer monsoon. *J. Geophys. Res.*, **107**, 4336, https://doi.org/10.1029/2001JD000382.

——, and Coauthors, 2001: BOBMEX: The Bay of Bengal Monsoon Experiment. *Bull. Amer. Meteor. Soc.*, **82**, 2217–2243, https://doi.org/10.1175/1520-0477(2001)082<2217:BTBOBM>2.3.CO;2.

Bigorre, S. P., R. A. Weller, J. B. Edson, and J. D. Ware, 2013: A surface mooring for air–sea interaction research in the Gulf Stream. Part II: Analysis of the observations and their accuracies. *J. Atmos. Oceanic Technol.*, **30**, 450–469, https://doi.org/10.1175/JTECH-D-12-00078.1.

Colbo, K., and R. A. Weller, 2009: The accuracy of the IMET sensor package in the subtropics. *J. Atmos. Oceanic Technol.*, **26**, 1867–1890, https://doi.org/10.1175/2009JTECHO667.1.

Dey, D., S. Sil, S. Jana, S. Pramanik, and P. C. Pandey, 2017: An assessment of TropFlux and NCEP air–sea fluxes on ROMS simulations over the Bay of Bengal region. *Dyn. Atmos. Oceans*, **80**, 47–61, https://doi.org/10.1016/j.dynatmoce.2017.09.002.

Fairall, C. W., E. F. Bradley, J. S. Godfrey, G. A. Wick, J. B. Edson, and G. S. Young, 1996: Cool-skin and warm-layer effects on sea surface temperature. *J. Geophys. Res.*, **101**, 1295–1308, https://doi.org/10.1029/95JC03190.

——, ——, J. E. Hare, A. A. Grachev, and J. B. Edson, 2003: Bulk parameterization of air–sea fluxes: Updates and verification for the COARE algorithm. *J. Climate*, **16**, 571–591, https://doi.org/10.1175/1520-0442(2003)016<0571:BPOASF>2.0.CO;2.

Gosnell, R., C. W. Fairall, and P. J. Webster, 1995: The sensible heat flux of rainfall in the tropical ocean. *J. Geophys. Res.*, **100**, 18 437–18 442, https://doi.org/10.1029/95JC01833.

Hosom, D. S., R. A. Weller, R. E. Payne, and K. E. Prada, 1995: The IMET (improved meteorology) ship and buoy systems.

J. Atmos. Oceanic Technol., **12**, 527–540, https://doi.org/10.1175/1520-0426(1995)012<0527:TIMSAB>2.0.CO;2.

Houze, R. A., 2004: Mesoscale convective systems. *Rev. Geophys.*, **42**, RG4003, https://doi.org/10.1029/2004RG000150.

IMD, 2015: Cyclonic storm Komen over the Bay of Bengal (26 July–02 August, 2015): A report. Indian Meteorological Department, 49 pp., http://www.rsmcnewdelhi.imd.gov.in/images/pdf/publications/preliminary-report/KOM.pdf.

List, R. J., 1984: *Smithsonian Meteorological Tables*. Smithsonian Institution Press, 527 pp.

Lorbacher, K., D. Dommenget, P. P. Niller, and A. Kohl, 2006: Ocean mixed layer depth: A subsurface proxy of ocean–atmosphere variability. *J. Geophys. Res.*, **107**, C07010, https://doi.org/10.1029/2003JC002157.

Lotliker, A. A., M. M. Omand, A. J. Lucas, S. R. Laney, A. Mahadevan, and M. Ravichandran, 2016: Penetrative radiative flux in the Bay of Bengal. *Oceanography*, **29** (2), 214–221, https://doi.org/10.5670/oceanog.2016.53.

Mahadevan, A., T. Paluskiewicz, M. Ravichandran, D. Sengupta, and A. Tandon, 2016: Introduction to the special issue on the Bay of Bengal: From monsoons to mixing. *Oceanography*, **29** (2), 14–17, https://doi.org/10.5670/oceanog.2016.34.

McPhaden, M. J., and Coauthors, 2009: RAMA: The Research Moored Array for African–Asian–Australian Monsoon Analysis and Prediction. *Bull. Amer. Meteor. Soc.*, **90**, 459–480, https://doi.org/10.1175/2008BAMS2608.1.

Murakami, T., 1979: Scientific objectives of the Monsoon Experiment (MONEX). *GeoJournal*, **3**, 117–136, https://doi.org/10.1007/BF00257701.

Narvekar, J., and S. P. Kumar, 2006: Seasonal variability of the mixed layer in the central Bay of Bengal and associated changes in nutrients and chlorophyll. *Deep-Sea Res. I*, **53**, 820–835, https://doi.org/10.1016/j.dsr.2006.01.012.

Paulson, C. A., and J. J. Simpson, 1977: Irradiance measurements in the upper ocean. *J. Phys. Oceanogr.*, **7**, 952–956, https://doi.org/10.1175/1520-0485(1977)007<0952:IMITUO>2.0.CO;2.

Prytherch, J., J. T. Farrar, and R. A. Weller, 2013: Observations and models of the diurnal warm layer. *J. Geophys. Res. Oceans*, **118**, 4553–4569, https://doi.org/10.1002/jgrc.20360.

Sengupta, D., B. N. Goswami, and R. Senan, 2001: Coherent intraseasonal oscillations of ocean and atmosphere during the Asian summer monsoon. *Geophys. Res. Lett.*, **28**, 4127–4130, https://doi.org/10.1029/2001GL013587.

——, G. N. Bharath Raj, and S. S. C. Shenoi, 2006: Surface freshwater from Bay of Bengal runoff and Indonesian Throughflow in the tropical Indian Ocean. *Geophys. Res. Lett.*, **33**, L22609, https://doi.org/10.1029/2006GL027573.

——, ——, M. Ravichandran, J. Sree Lekha, and F. Papa, 2016: Near-surface salinity and stratification in the north Bay of Bengal from moored observations. *Geophys. Res. Lett.*, **43**, 4448–4456, https://doi.org/10.1002/2016GL068339.

Torrence, C., and G. P. Compo, 1998: A practical guide to wavelet analysis. *Bull. Amer. Meteor. Soc.*, **79**, 61–78, https://doi.org/10.1175/1520-0477(1998)079<0061:APGTWA>2.0.CO;2.

Vecchi, G. B., and D. E. Harrison, 2002: Monsoon breaks and subseasonal sea surface temperature variability in the Bay of Bengal. *J. Climate*, **15**, 1485–1493, https://doi.org/10.1175/1520-0442(2002)015<1485:MBASSS>2.0.CO;2.

Venkatesan, R., V. R. Shamji, G. Latha, S. Mathew, R. R. Rao, A. Muthiah, and M. A. Atmanand, 2013: In situ ocean subsurface time series from OMNI buoy network in the Bay of Bengal. *Curr. Sci.*, **104**, 1166–1177, http://www.currentscience.ac.in/Volumes/104/09/1166.pdf.

Webster, P. J., and Coauthors, 2002: The JASMINE pilot study. *Bull. Amer. Meteor. Soc.*, **83**, 1603–1630, https://doi.org/10.1175/BAMS-83-11-1603.

Weller, R. A., 2015: Variability and trends in surface meteorology and air–sea fluxes at a site off northern Chile. *J. Climate*, **28**, 3004–3023, https://doi.org/10.1175/JCLI-D-14-00591.1.

——, and S. P. Anderson, 1996: Surface meteorology and air–sea fluxes in the western equatorial Pacific warm pool during the TOGA Coupled Ocean-Atmosphere Response Experiment. *J. Climate*, **9**, 1959–1990, https://doi.org/10.1175/1520-0442(1996)009<1959:SMAASF>2.0.CO;2.

——, S. Majumder, and A. Tandon, 2014: Diurnal restratification events in the Southeast Pacific trade wind regime. *J. Phys. Oceanogr.*, **44**, 2569–2587, https://doi.org/10.1175/JPO-D-14-0026.1.

——, and Coauthors, 2016: Air–sea interaction in the Bay of Bengal. *Oceanography*, **29** (2), 28–37, https://doi.org/10.5670/oceanog.2016.36.

Yu, L., X. Jin, and R. A. Weller, 2007: Annual, seasonal, and interannual variability of air–sea heat fluxes in the Indian Ocean. *J. Climate*, **20**, 3190–3209, https://doi.org/10.1175/JCLI4163.1.